



Spatiotemporal single-cell roadmap of human skin wound healing

Downloaded from: <https://research.chalmers.se>, 2025-05-09 15:06 UTC

Citation for the original published paper (version of record):

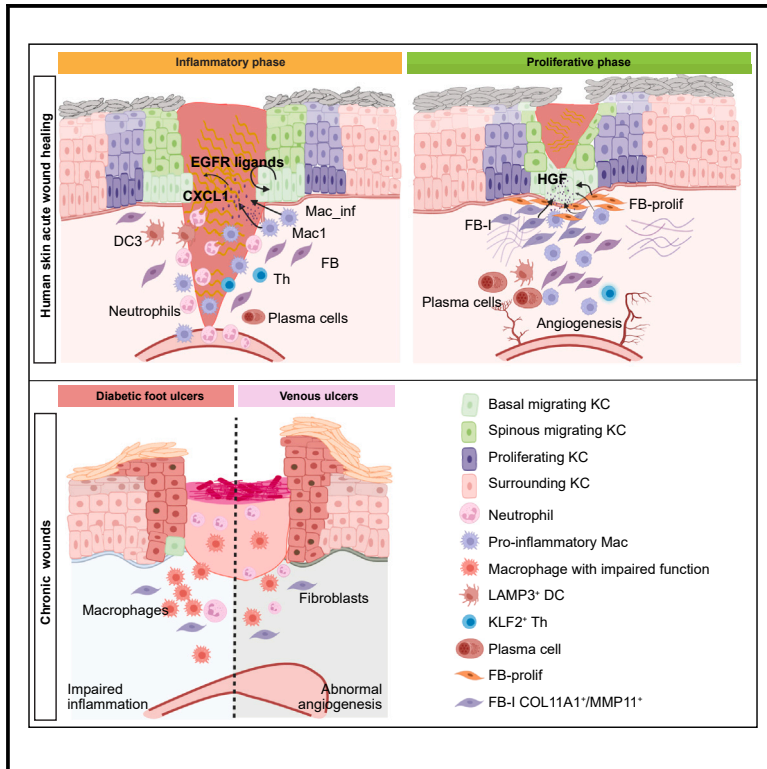
Liu, Z., Bian, X., Luo, L. et al (2025). Spatiotemporal single-cell roadmap of human skin wound healing. *Cell Stem Cell*, 32(3): 479-498.e8. <http://dx.doi.org/10.1016/j.stem.2024.11.013>

N.B. When citing this work, cite the original published paper.

Cell Stem Cell

Spatiotemporal single-cell roadmap of human skin wound healing

Graphical abstract



Authors

Zhuang Liu, Xiaowei Bian,
Lihua Luo, ..., Pehr Sommar,
Dongqing Li, Ning Xu Landén

Correspondence

dongqing.li@pumcdern.cams.cn (D.L.),
ning.xu@ki.se (N.X.L.)

In brief

Xu Landén and colleagues conducted a unique study on human skin wound healing by inducing wounds in healthy donors and collecting wound-edge tissues at three healing stages. Transcriptome profiling from this study deepens our understanding of tissue repair mechanisms, paving the way for novel therapeutic targets to treat chronic wounds.

Highlights

- A spatiotemporal atlas to explore human *in vivo* gene expression across wound healing
- Wound margin architecture unveils a model for human re-epithelialization
- Distinct healing challenges in venous ulcers and diabetic foot ulcers
- Unique human healing traits emerge in cellular heterogeneity and gene expression



Resource

Spatiotemporal single-cell roadmap of human skin wound healing

Zhuang Liu,¹ Xiaowei Bian,¹ Lihua Luo,¹ Åsa K. Björklund,^{3,4} Li Li,² Letian Zhang,¹ Yongjian Chen,¹ Lei Guo,² Juan Gao,² Chunyan Cao,² Jiating Wang,² Wenjun He,⁵ Yunting Xiao,² Liping Zhu,² Karl Annusver,⁶ Nusayhah Hudaa Gopee,⁷ Daniela Basurto-Lozada,^{7,8} David Horsfall,^{7,8} Clare L. Bennett,¹⁰ Maria Kasper,⁶ Muzlifah Haniffa,^{7,8,9} Pehr Sommar,¹¹ Dongqing Li,^{2,*} and Ning Xu Landén^{1,12,*}

¹Dermatology and Venerology Division, Department of Medicine Solna, Center for Molecular Medicine, Karolinska Institutet, 17176 Stockholm, Sweden

²Key Laboratory of Basic and Translational Research on Immune-Mediated Skin Diseases, Chinese Academy of Medical Sciences, Jiangsu Key Laboratory of Molecular Biology for Skin Diseases and STIs, Institute of Dermatology, Chinese Academy of Medical Sciences and Peking Union Medical College, 210042 Nanjing, China

³Department of Life Science, National Bioinformatics Infrastructure Sweden, Göteborg, Sweden

⁴Science for Life Laboratory, Chalmers University of Technology, 41296 Göteborg, Sweden

⁵The first affiliated hospital of Soochow University, Department of Plastic and Burn Surgery, NO.188, Shizi Street, Suzhou, Jiangsu, China

⁶Department of Cell and Molecular Biology, Karolinska Institutet, 17177 Stockholm, Sweden

⁷Biosciences Institute, Newcastle University, Newcastle upon Tyne NE2 4HH, UK

⁸Wellcome Sanger Institute, Wellcome Genome Campus, Hinxton, Cambridge CB10 1SA, UK

⁹Department of Dermatology and NIHR Newcastle Biomedical Research Centre, Newcastle Hospitals NHS Foundation Trust, Newcastle upon Tyne NE1 4LP, UK

¹⁰Department of Haematology, University College London (UCL) Cancer Institute, London WC1E 6DD, UK

¹¹Department of Plastic and Reconstructive Surgery, Karolinska University Hospital, 17176 Stockholm, Sweden

¹²Lead contact

*Correspondence: dongqing.li@pumcderm.cams.cn (D.L.), ning.xu@ki.se (N.X.L.)

<https://doi.org/10.1016/j.stem.2024.11.013>

SUMMARY

Wound healing is vital for human health, yet the details of cellular dynamics and coordination in human wound repair remain largely unexplored. To address this, we conducted single-cell multi-omics analyses on human skin wound tissues through inflammation, proliferation, and remodeling phases of wound repair from the same individuals, monitoring the cellular and molecular dynamics of human skin wound healing at an unprecedented spatiotemporal resolution. This singular roadmap reveals the cellular architecture of the wound margin and identifies *FOSL1* as a critical driver of re-epithelialization. It shows that pro-inflammatory macrophages and fibroblasts sequentially support keratinocyte migration like a relay race across different healing stages. Comparison with single-cell data from venous and diabetic foot ulcers uncovers a link between failed keratinocyte migration and impaired inflammatory response in chronic wounds. Additionally, comparing human and mouse acute wound transcriptomes underscores the indispensable value of this roadmap in bridging basic research with clinical innovations.

INTRODUCTION

Wound healing is a vital process for skin integrity, progressing through three overlapping phases: inflammation, proliferation, and remodeling.^{1,2} These stages are driven by complex interactions among diverse cell types. Re-epithelialization, crucial during the proliferation phase, requires the migration and proliferation of epidermal keratinocytes to cover the wound. Failed re-epithelialization is a common issue in chronic wounds like diabetic foot ulcers (DFUs) and venous ulcers (VUs), impacting millions globally each year.³ There's an urgent need for more effective wound therapies, yet progress is hindered by limited knowledge of human skin wound healing. While animal models,

mainly rodents, have provided foundational insights, significant anatomical and physiological differences between humans and rodents limit their applicability, often resulting in high clinical trial failure rates for treatments.^{4,5}

Significant efforts have been made to analyze pathological wounds, such as pressure ulcers⁶ and DFUs^{7,8} as well as pathological scars,^{9–11} using single-cell RNA sequencing (scRNA-seq) and spatial transcriptomic sequencing (ST-seq), as these samples are more readily obtained during treatment. However, a comprehensive cellular atlas detailing normal skin wound healing in humans over time is still missing. This knowledge gap is crucial for identifying critical cellular and molecular mediators of wound healing, understanding obstacles to healing in chronic



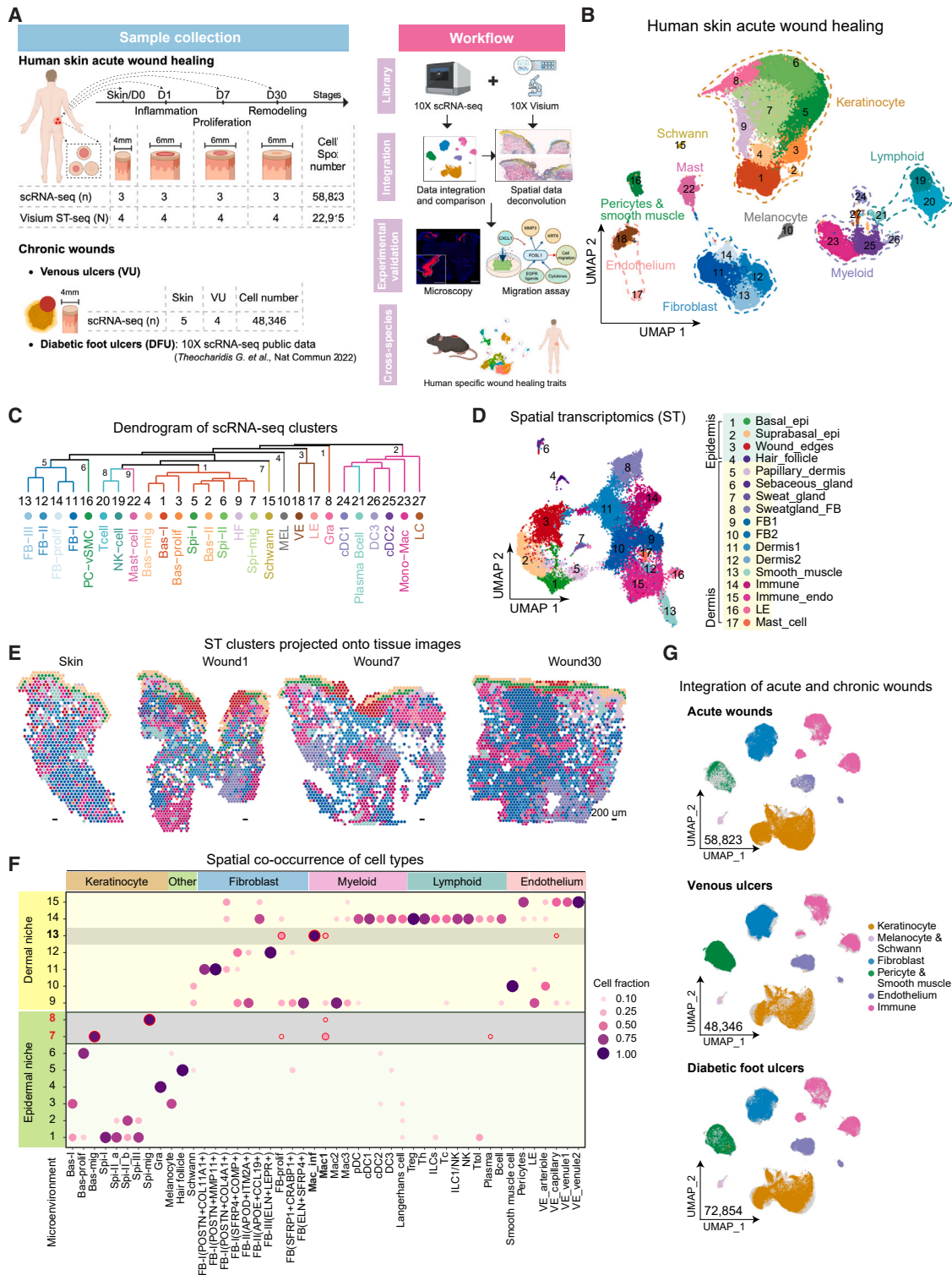


Figure 1. A spatiotemporal map of human skin wound healing

(A) Schematic outline of the study.
 (B) UMAP of human acute wound (ACW) scRNA-seq.
 (C) Dendrogram illustrating cell clusters' relatedness based on gene expression.
 (D) UMAP of human ACW ST-seq.
 (E) Spatial projection of cell types onto hematoxylin and eosin (H&E) images of human ACWs. Donor 2 is shown.

(legend continued on next page)

wounds, and validating the clinical relevance of findings from animal and *in vitro* models.

In this study, we utilized scRNA-seq and ST-seq to monitor gene expression dynamics at the single-cell level across different healing phases. These efforts led to the development of a comprehensive spatiotemporal cell atlas of human skin wound healing, accessible for interactive exploration online (<https://www.xulandenlab.com/tools>). Through this atlas, we identified an epidermal wound margin structure and fundamental regulatory mechanisms driving re-epithelialization in humans. Our comparative studies with chronic wounds revealed diverse pathological changes specific to their causes and prognoses. Additionally, the comparison of human and mouse acute wound transcriptomes showed both shared and unique healing mechanisms, highlighting this atlas's crucial role in translating fundamental discoveries into therapeutic approaches.

RESULTS

A spatiotemporal map of human skin wound healing

In this study, we collected samples from pre-wound intact skin and the entire concentric wound-edge 1 (Wound1), 7 (Wound7), and 30 days (Wound30) post-injury, all from the same individuals (Figure 1A; Table S1). This approach ensures that the data reflect the healing process consistently within individual biological contexts rather than introducing variability by comparing different stages from different donors. We analyzed serial human acute wound samples from three donors using scRNA-seq and four donors using Visium ST-seq. Biopsies from two donors were analyzed using both techniques. Using pseudo-bulk principal component analysis and sample similarity analysis in scRNA-seq (Figure S1A) and between scRNA-seq and ST-seq data (Figure S2A) without batch correction, we found that samples cluster by conditions rather than by donors or experimental methods. This indicates low patient heterogeneity in the study, making it suitable for analyzing biological differences across healing stages.

Next, we defined the healing stages of each acute wound sample based on key biological events in wound repair.² Gene Ontology (GO) analysis of differentially expressed genes (DEGs) in our scRNA-seq data showed that Wound1 was enriched in granulocyte chemotaxis, RNA metabolism, and ATP biosynthesis, indicating inflammation (Figure S1B). By day 7, DEGs related to nuclear division and extracellular matrix (ECM) organization marked the proliferative phase, while Wound30 DEGs involved in ECM, neuron, and sensory system development indicated tissue remodeling. These findings align with our previous bulk RNA-seq¹² results and histological analysis (Figure S2F). Comparing our scRNA-seq data with public bulk RNA-seq and microarray datasets of human and mouse skin wounds^{13–15} confirmed similar sequential wound-healing re-

sponses (Figures S1C and S1D). Thus, Wound1, Wound7, and Wound30 represent the inflammatory, proliferative, and remodeling phases, respectively.

After removing doublets^{16,17} and low-quality cells, a total of 58,823 cells from human acute wounds remained (Figures S1E–S1G). Using graph-based clustering with Louvain algorithm,¹⁸ we identified 27 cell clusters, which were further grouped into nine main cell types based on DEGs and known markers^{19,20}: keratinocytes (*KRT5*^{high} or *KRT10*^{high}), fibroblasts (FBs) (*COL1A1*⁺), myeloid cells (*LYZ*⁺ and *HLA-DRA*⁺), lymphoid cells (*CD3D*⁺ or *NKG7*⁺), endothelial cells (*PECAM1*⁺), mast cells (*TPSAB1*⁺ and *TPSB2*⁺), pericytes and smooth muscle cells (*ACTA2*⁺ and *MYH11*⁺), melanocytes (*TYRP1*⁺ and *PMEL*⁺), and Schwann cells (*SOX10*⁺ and *SOX2*⁺) (Figures 1B, 1C, and S1H; Table S2). Integration and comparison with public scRNA-seq data from human adult skin confirmed the accuracy and comprehensiveness of our cell-type annotations (Figures S1I and S1J).²⁰

ST-seq analysis of human acute wounds identified 22,915 spots, clustered into 17 populations (Figures 1D, 1E, and S2B–S2E; Table S2). The epidermal compartment included basal keratinocytes (*KRT15*⁺ and *COL17A1*⁺), suprabasal cells (*KRT1*⁺, *KRT2*⁺, and *LORICRIN*⁺), hair follicles (*HR*⁺, *FZD7*⁺, and *KRT75*⁺),^{21,22} and a wound-edge cluster (*KRT6A/B/C*⁺, *KRT16*⁺, *KRT17*⁺, and *S100A8/9*⁺). The dermal clusters comprised FBs (*ADAM12*⁺, *POSTN*⁺, *MMP2*⁺, and *FBLN1*⁺),^{23,24} sweat glands (*KRT77*⁺, *DCD*⁺, *SCGB1D2*⁺, and *MUCL1*⁺),²⁵ sebaceous glands (*MGS11*⁺, *FADS2*⁺, and *KRT79*⁺),^{21,22} immune cells (*FABP4*⁺, *CD36*⁺, and *CD163*⁺), endothelial cells (*VWF*⁺, *CD74*⁺, *CCL21*⁺, and *LYVE1*⁺), smooth muscle cells (*MYL9*⁺ and *TAGLN*⁺),²⁶ and a mast cell cluster (*TPSB2*⁺ and *MS4A2*⁺).

To map the spatial positions of scRNA-seq-identified cells in their native environments, we performed Cell2location analysis²⁷ in ST-seq, creating a spatiotemporal atlas of human skin wound healing. Non-negative matrix factorization allowed us to distinguish epidermal and dermal niches, revealing cell colocalization at different healing stages (Figures 1F and S2F). For example, niches 6, 7, and 8 mark the re-epithelialization process, peaking at Wound1 and Wound7; niche 13 reflects granulation tissue, peaking at Wound7; niche 11 increases at Wound30, indicating scar formation; and niche 15, involved in angiogenesis, peaks at Wound7 and Wound30. These microenvironments highlight spatially restricted cell-to-cell communication during healing, particularly interactions between macrophages and both migrating keratinocytes (niches 7 and 8) and proliferating FBs (niche 13), underscoring the role of wound inflammation in repair beyond infection defense and debris clearance.

Furthermore, to deepen our understanding of chronic wound pathology, we performed scRNA-seq on VU biopsies from four patients, with each biopsy consisting of 50% wound-edge and 50% wound-bed tissues (Figure 1A; Table S1), as well as five

(F) Dot plot showing spatial co-occurrence analysis of deconvoluted cell types using non-negative matrix factorization (NMF) method. Dot size and color represent cell fractions normalized across niches for each cell type.

(G) UMAP of main cell types in integrated human acute and chronic wound scRNA-seq datasets. Bas-/Spi-/Gra-, basal/spinose/granular keratinocyte; -prolif/-mig, proliferating/migrating cells; HF, hair follicle; MEL, melanocyte; FB, fibroblast; Mono-mac, monocyte and macrophage; Mac_infl, inflammatory macrophage; cDC/pDC, conventional/plasmacytoid dendritic cell; LC, Langerhans cell; NK-cell, natural killer cell; Th, T helper cell; Treg/Tc/Ttol, regulatory/cytotoxic/tolerant T cell; ILC, innate lymphoid cell; PC-vSMC, pericyte and vascular smooth muscle cell; LE/VE, lymphatic/vascular endothelial cell.

See also Tables S1 and S2.

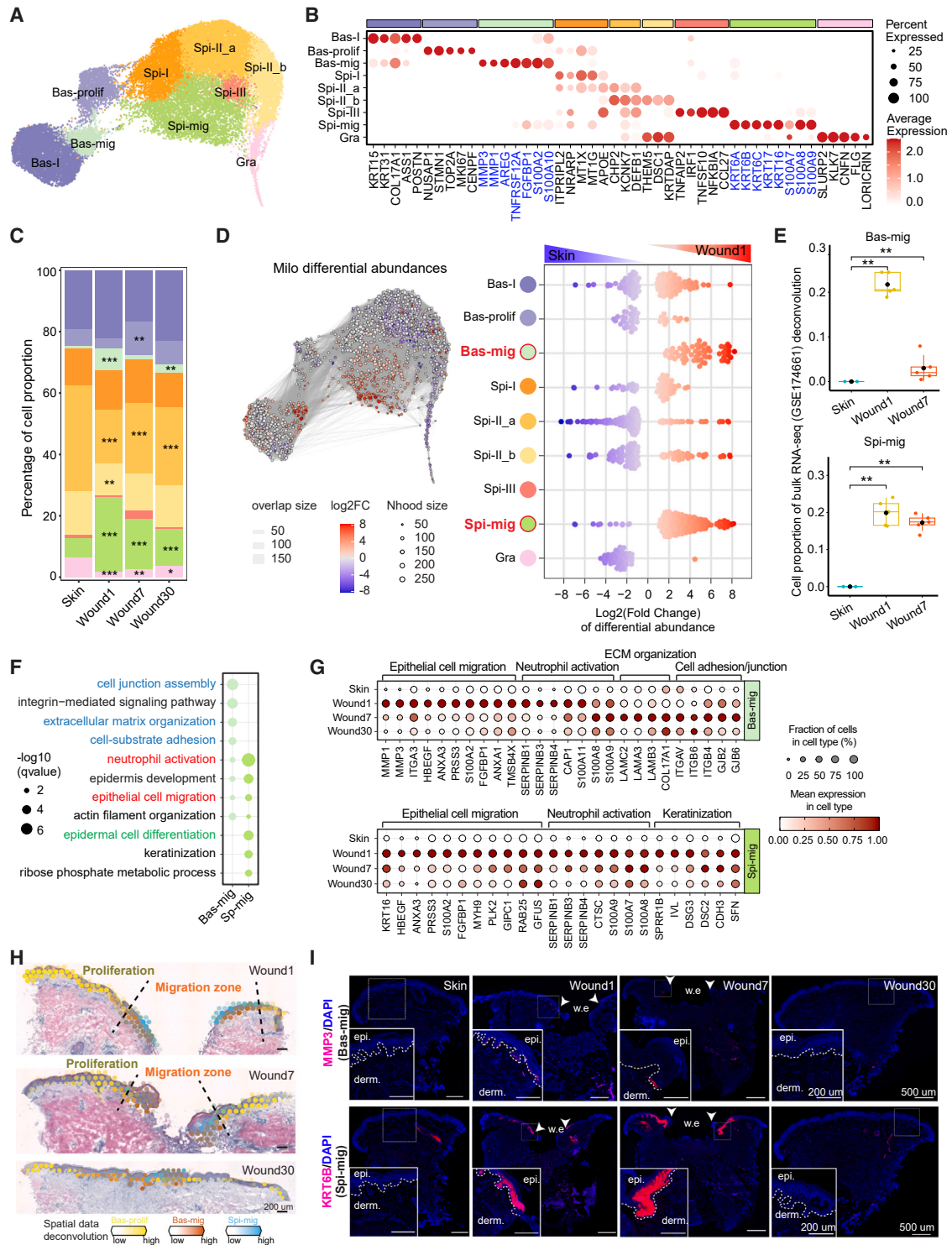


Figure 2. Spatiotemporal dissection of human wound re-epithelialization

(A) UMAP of keratinocyte (KC) subclusters.

(B) Dot plot of marker gene expression.

(C) Cell proportions of each sub-cluster.

(D) Milo analysis of keratinocyte abundance difference between Wound1 and skin. Left panel shows the graph representation of neighborhoods. The node size and edges are proportional to the number of cells and overlapped cell numbers between any two nodes, respectively. Nodes are colored by \log_2 (fold changes) of cell abundance between conditions. Right panel shows the distribution of neighborhood abundance in cell types by beeswarm plot. Blue and red dots indicate

(legend continued on next page)

control skin samples. We integrated scRNA-seq data from human acute wounds with data from VU and public DFU data⁷ using Harmony²⁸ (Figures 1G, S1K, and S1L). Notably, the DFU study compared foot skin from nine non-diabetic individuals to DFU wound-edge tissues from 11 diabetic patients. These DFU cases were divided into two groups based on 12-week healing outcomes: healed (DFU_H, $n = 7$) and non-healed (DFU_NH, $n = 4$).⁷ This integration allows us to directly compare human acute wounds to chronic wounds of different etiologies and identify pathological barriers that hinder wound closure.

Spatiotemporal dissection of human wound re-epithelialization

Recognizing that impaired re-epithelialization is a common challenge in pathological wounds,³ our study aimed to better understand this process in human wounds. Using scRNA-seq, we classified keratinocytes from human acute wounds into nine subclusters (Figures 2A and 2B; Table S3), including three basal types: Bas-I cells (*ASS1*⁺ and *POSTN*⁺), a proliferating type (Bas-prolif: *STMN1*⁺ and *TOP2A*⁺), and a migrating type (Bas-mig) expressing matrix metalloproteinases (*MMPs*) and *FGFBP1*; five spinous (Spi) types: ranging from Spi-I/IIa/b with metallothionein expression to Spi-III with immune response genes (*TNFSF10*, *IRF*, and *CCL27*), and a migrating spinous cluster (Spi-mig) expressing *KRT6* genes and S100 proteins; a granular cluster (Gra) displaying late differentiation markers (*FLG* and *LORICRIN*). Analysis of cell proportions and graph-based differential abundance testing using Milo²⁹ revealed a notable early increase in migrating keratinocytes (Bas-mig and Spi-mig) during the initial inflammatory phase of wound healing (Wound1). This increase is contrasted by a decrease in differentiated keratinocytes (Spi-II and Gra), compared with normal skin (Figures 2C, 2D, and S3A). These observations were supported by deconvolution analysis of our prior bulk RNA-seq data using the same *in vivo* human wound-healing model¹² (Figures 2E and S3B). Additionally, we noted increased proliferating keratinocytes at Wound7, suggesting a robust proliferative response to facilitate wound healing (Figures 2C and S3C).

Upon examining the migrating keratinocytes, we found that both Bas-mig and Spi-mig clusters expressed genes essential for epithelial cell migration (e.g., *HBEGF*, *ANXA3*, *PRSS3*, *S100A2*, and *FGFBP1*) and neutrophil activation (e.g., *SERPINE1/3/4* and *S100A7/8/9/11*), as shown by GO analysis (Figure 2F; Table S3). These genes peaked during the inflammatory phase (Wound1) (Figure 2G). In the subsequent proliferative phase (Wound7), Bas-mig keratinocytes exhibited increased expression of ECM organization and cell adhesion-related genes (e.g., laminin 5, integrins, and collagen), indicative of late stages

of re-epithelialization where cell-to-cell and cell-to-matrix adhesions are re-established (Figure 2G). Deconvolution results revealed Spi-mig overlaying Bas-mig at the wound leading edge, surrounded by Bas-prolif (Figure 2H). This cellular arrangement forms rapidly post-injury, intensifies during the proliferative phase, and recedes by the remodeling phase (Wound30) (Figure 2H). This pattern was further confirmed in additional human wound tissues through RNA-fluorescence *in situ* hybridization (FISH) and spatial gene expression (Figures 2I and S3D).

To identify keratinocytes directly involved in wound repair, we sorted all scRNA-seq-analyzed keratinocytes from acute wounds into two groups using a Gaussian mixture model: 10,064 wound-associated (*KRT6A*⁺) and 17,041 non-wound (*KRT6A*^{-/dim}) cells (Figure S3E). We targeted *KRT6A* expression as a marker for post-injury keratinocytes,^{30,31} which was validated by pronounced *KRT6A* expression in wound-edge keratinocytes observed in ST-seq, in contrast to its absence in intact skin (Figure S3F). Pseudotemporal analysis traced a differentiation pathway from basal to spinous and then to granular keratinocytes for both wound and non-wound cells (Figures 3A and 3B). Notably, within the wound-associated group, two additional branches emerged: one transitioning from Bas-I to Bas-mig and another from Spi-II to Spi-mig, suggesting that these migrating cells originate from wound-edge keratinocytes with respective differentiation states (Figure 3B).

In summary, our study suggests a model of re-epithelialization in human wounds, characterized by organized keratinocyte proliferation, differentiation, and migration. Mirroring recent findings in murine skin,^{32,33} we identified two distinct zones of epidermal cells around the wound: a non-proliferative migrating front surrounded by a highly proliferative hub. In contrast to murine wounds, where migrating keratinocytes often proliferate, creating a mixed zone,^{33,34} human wounds show a distinct separation between keratinocyte proliferation and migration (Figure S3G).

Gene network interference identifies *FOSL1* as a key driver of keratinocyte migration

To compare gene regulatory networks in various keratinocyte states during homeostasis and wound repair, we analyzed genes showing significant expression changes along trajectories of wound and non-wound keratinocytes, categorizing them by their expression pattern (Figure 3C). GO analysis revealed that both wound and non-wound keratinocytes share several GO term patterns, including cell-substrate adhesion (I), nuclear division (II), ribosome biogenesis/epidermal development (III), and keratinization (V), indicating a common differentiation path. Notably, non-wound keratinocytes, especially toward the end of their

significantly (SpatialFDR < 0.1) decreased (logFC < 0) and increased (logFC > 0) cell abundance, respectively. Color intensity indicates the degree of significance for each neighborhood.

(E) Cellular proportions of deconvoluted Bas-/Spi-mig in public bulk RNA-seq data (GSE174661).

(F) GO plot of biological process (BP) terms enriched in Bas-mig and Spi-mig using the top 200 markers.

(G) Dot plots showing the expression of genes in (F) GO terms.

(H) Deconvoluted Bas-prolif, Bas-mig, and Spi-mig in ST-seq showing distinctive migration and proliferation zones at wound edges. Donor 2 is shown.

(I) Fluorescence *in situ* hybridization (FISH) images of *MMP3* (upper) and *KRT6B* (lower) expressions during wound healing. Scale bar, 500 μ m, inset plot scale bar, 200 μ m. Significance was assessed using generalized linear modeling on a quasi-binomial distribution (C) and Mann-Whitney U test (E), * $p < 0.05$, ** $p < 0.01$, *** $p < 0.001$.

See also Table S3.

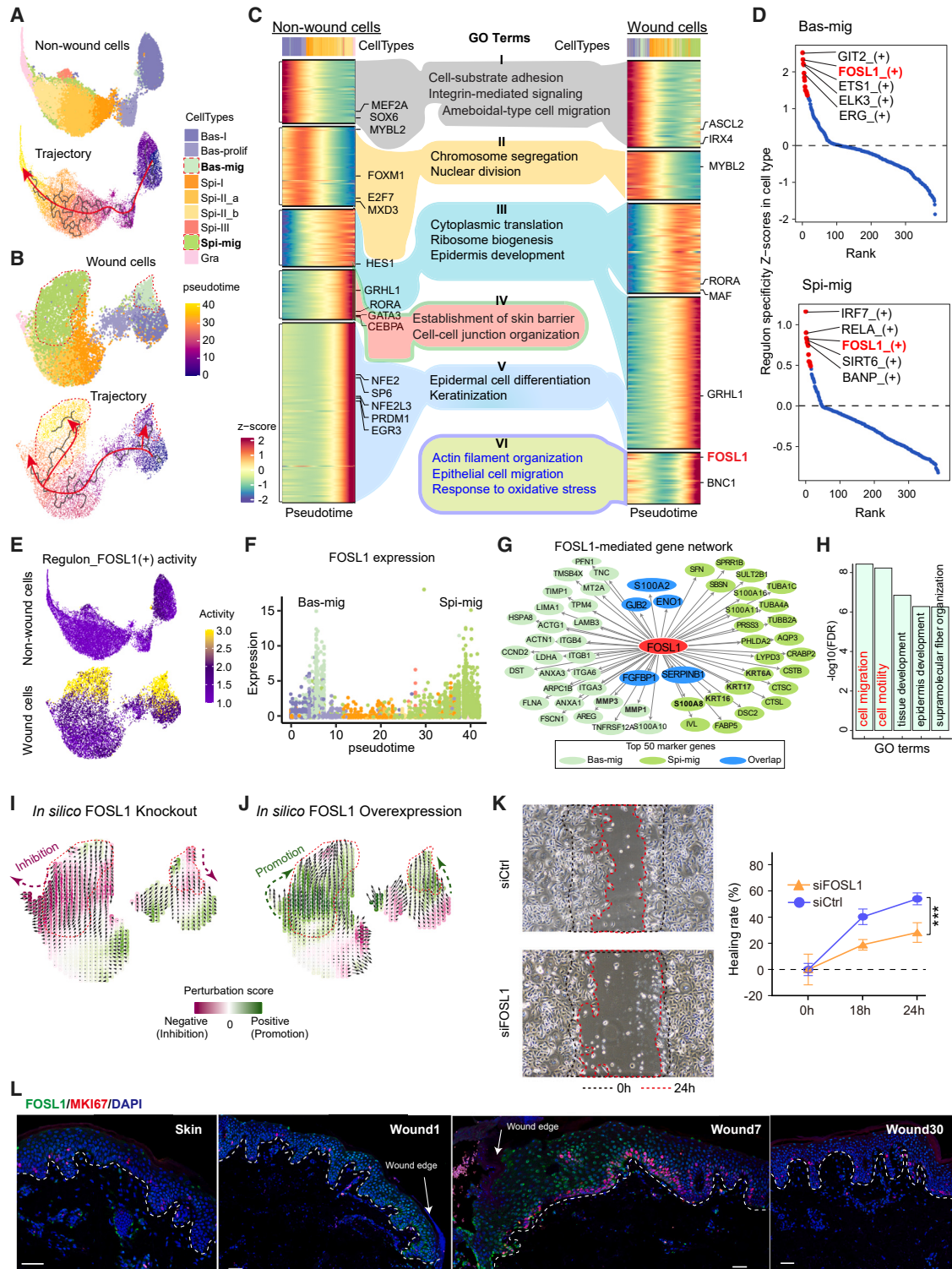


Figure 3. Gene network interference identifies *FOSL1* as a key driver of keratinocyte migration

(A and B) UMAP of cell clusters (upper) and pseudotime trajectories (lower) in non-wound (A) and wound keratinocytes (B).

(C) Heatmaps of driving gene expressions along the pseudotime. Transcription factors (TFs) are labeled on the right. GO terms of different patterns are shown in the middle.

(D) Scatter plots of top 5 TF regulons based on specificity Z scores in Bas-mig (top) and Spi-mig (bottom).

(E) UMAP of *FOSL1* regulon activity in non-wound and wound cells.

(F) *FOSL1* gene expression along with pseudotime.

(legend continued on next page)

trajectory (e.g., Spi-II/Gra), expressed genes linked to skin barrier formation and cell-to-cell junctions (IV), which were absent in wound keratinocytes. Conversely, wound keratinocytes displayed a unique expression pattern (VI) involving epithelial migration, actin organization, and oxidative stress response, prominently seen in Bas-mig and Spi-mig at the trajectory's start and end, respectively (Figure 3C).

Combining pseudotime analysis with SCENIC analysis³⁵ to explore gene regulatory networks driving the migrating keratinocyte phenotype, we identified *FOSL1* as a critical master regulator in both Bas-mig and Spi-mig clusters (Figures 3C and 3D; Table S3). *FOSL1*, a vital component of the AP1 transcriptional complex, is involved in cell differentiation, stress response, and cancer metastasis^{36,37}; however, its specific role in keratinocyte behavior during wound healing was unclear.³⁸ We observed that *FOSL1* exhibited high regulatory and expression specificity in migrating cells (Figures 3E and 3F), and GO analysis of *FOSL1*-targeted genes in these clusters underscored their crucial role in cell migration (Figures 3G and 3H; Table S3).

To better understand the impact of *FOSL1* perturbations on keratinocyte cell states in human wounds, we used the CellOracle package.³⁹ Our *in silico* analysis showed that disrupting *FOSL1* impeded the migratory state of keratinocytes while enhancing *FOSL1* promoted their migratory phenotype (Figures 3I and 3J). These computational predictions were experimentally validated: silencing *FOSL1* with siRNA significantly reduced the motility of human keratinocyte progenitors in a scratch assay (Figures 3K and S3H). Together, both *in silico* and experimental findings highlight *FOSL1*'s crucial role in regulating keratinocyte mobility.

Consistent with its role in cell migration, *FOSL1* was transiently upregulated in basal and suprabasal keratinocytes at wound edges compared with the intact skin, as shown by our scRNA-seq and ST-seq data and confirmed by immunofluorescence (IF) staining (Figures 3L, S3I, and S3J). This upregulation also occurred in the wound-edge keratinocytes in a mouse acute wound model, suggesting an evolutionarily conserved role in keratinocyte migration (Figure S3K).

Pro-inflammatory macrophages support re-epithelialization at the inflammatory phase

Our combined scRNA-seq and ST-seq analysis extends beyond keratinocytes, revealing the dynamic gene expression and cellular diversity of immune cells, FBs, and angiogenic cells throughout human skin wound healing. We identified 11 myeloid cell types in acute wounds, including four macrophage clusters: Mac_inf (*APOE*⁺ and *CXCL1*⁺), Mac1 (*IL1B*⁺, *THBS1*⁺, and *EREG*⁺), Mac2 (*DAB2*⁺ and *C1QA/B*⁺), and Mac3 (*MMP19*⁺, *MMP9*⁺, and *VEGFA*⁺)^{40,41}; four dendritic cell clusters: plasmacytoid DC (pDC, *ACOT7*⁺, *LTB*⁺, and *IGKC*⁺), conventional DC1 (cDC1, *CLEC9A*⁺,

and *WDFY4*), cDC2 (*CD1C*⁺, *IL1R2*⁺, and *CLEC10A*⁺), and DC3 (*CCR7*⁺ and *LAMP3*⁺); Langerhans cells (LC: *CD207*⁺ and *CD1A*⁺); and subsets of apoptotic (*DNAJB1*⁺ and *HSPA1B*⁺) and cycling (*PCLAF*⁺ and *H4C3*⁺) cells (Figures 4A, 4B, and S4A; Table S4). Additionally, we identified neutrophils (*CSF3R*⁺, *FCGR3B*⁺, *CXCR2*⁺, and *CMTM2*⁺),⁴² which were initially missed in standard scRNA-seq analysis due to their low RNA content and high RNase levels (Figures S4B–S4H). We also identified nine clusters of lymphoid cells, including regulatory T cells (Treg: *TIGIT*⁺, *BATF*⁺, and *FOXP3*⁺), helper T cells (Th: *LDHB*⁺, *KLF2*⁺, and *GIMAP7*⁺), innate lymphoid cells (ILC: *AHR*⁺, *CCR6*⁺, and *PTGER4*⁺), cytotoxic T cells (Tc: *TRGC2*⁺ and *KLRC2/3*⁺), ILC1/natural killer cells (*XCL1/2*⁺ and *FCER1G*⁺), NK cells (*GZMA/K*⁺), tolerant T cells (Ttol: *DNAJB1*⁺ and *NR4A1*⁺),⁴³ plasma cells (*PTGDS*⁺, *JCHAIN*⁺, and *IL3RA*⁺), and B cells (*IGHM*⁺, *MS4A1*⁺, and *CD79A*⁺)^{20,43,44} (Figures 4F, 4G, and S4I; Table S4).

Macrophages are highly plastic, showing phase-specific activation during wound repair.^{45,46} Across healing stages, we observed a mix of pro-inflammatory and pro-resolution macrophages, with varying proportions and functions (Figures S4L and S4M). The relative proportion of pro-inflammatory macrophages (Mac_inf and Mac1) increased transiently in Wound1 and Wound7, marked by upregulation of HIF1 α and pro-inflammatory cytokines (tumor necrosis factor alpha [TNF- α], *IL-1 β* and *CCL2*) (Figure S4N).⁴⁶ In contrast, markers of pro-resolution macrophages (*MRC1*, *IL-10*, transforming growth factor β [TGF- β], and *PDGFB*) were downregulated early on (Figure S4O).⁴⁶ Recent studies have shown that macrophage metabolic reprogramming is key to wound healing.⁴⁷ Gene set enrichment analysis confirmed that early-phase macrophages (Wound1 and Wound7) were glycolytic, with a deficient tricarboxylic acid (TCA) cycle and enrichment in oxidative phosphorylation genes (Figure S4P). This enhanced glucose metabolism supports antibacterial functions like phagocytosis and reactive oxygen species production.⁴⁸ By Wound30, macrophages shifted from glycolysis to upregulate TCA cycle genes (Figure S4P).⁴⁷ This metabolic reprogramming was also reflected in four macrophage subtypes: pro-inflammatory macrophages favored glycolysis and oxidative phosphorylation, while pro-resolution macrophages were enriched in TCA cycle and amino acid metabolism genes, aligning with their roles in different healing stages (Figure S4Q).

Cell proportion and Milo²⁹ analyses highlighted several immune cells peaking during the inflammatory phase of wound repair: (1) pro-inflammatory macrophages (Mac_inf and Mac1) located in the upper dermis adjacent to migrating epithelial cells (Figures 4C–4E); (2) neutrophils, known as the first myeloid cells recruited from circulation (Figures S4G and S4H); (3) DC3 cells, noted for their maturity and migratory capabilities, with significant cytokine⁴⁹ (Figures 4C and 4D); and (4) Th cells, which lack clear differentiation markers but are unified by high expression of

(G) Top 50 marker genes of Bas-mig (light green), Spi-mig (green), and shared in clusters (blue) regulated by *FOSL1*.

(H–J) (H) GO terms of *FOSL1*-regulated genes shown in (G). Perturbation simulation vector fields in wound keratinocytes with *in silico* *FOSL1* knockout (I) or overexpression (J). The positive (green) and negative (purple) perturbation scores indicate promotion and inhibition of cell state change, respectively.

(K) Scratch wound assay of human primary keratinocytes with *FOSL1* expression silencing. Significance was determined using a one-way ANOVA test, ****p* < 0.001.

(L) Immunofluorescence staining of *FOSL1* and MKI67 in human acute wound healing. Dotted lines represent the boundary of the epidermis and dermis. DAPI stains the nuclei. Arrows represent wound edges. Scale bar, 50 μ m.

See also Table S3.

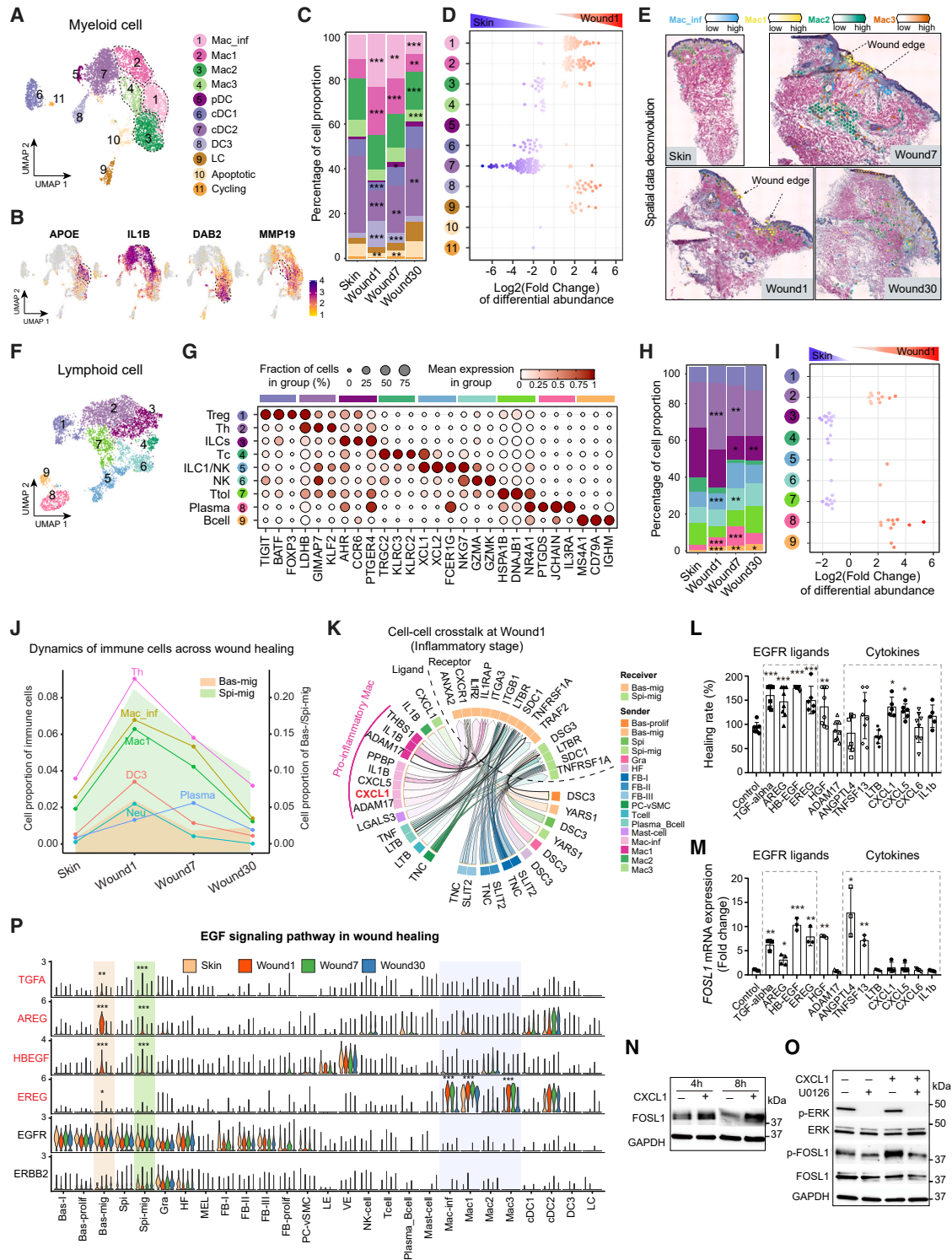


Figure 4. Pro-inflammatory macrophages support re-epithelialization at the inflammatory phase

(A) UMAP of myeloid subpopulations.

(B) Feature plots showing macrophage markers of *APOE* (Mac_inf), *IL1B* (Mac1), *DAB2* (Mac2), and *MMP19* (Mac3).

(C) Cell proportions of myeloid cell types.

(D) Milo beeswarm plot showing the differential abundance of cell types between Wound1 and skin. Blue and red dots indicate significantly decreased and increased cell abundance, respectively.

(E) Deconvoluted macrophages in ST-seq. Donor 3 is shown.

(legend continued on next page)

KLF2, a transcription factor regulating T cell migration and differentiation (Figures 4H, 4I, S4J, and S4K).⁵⁰ The lineage-negative *KLF2*⁺ Th cells are crucial for maintaining commensal tolerance and preventing microbiota-driven intestinal inflammation.⁵¹ Whether they play a similar immune-suppressive role in skin wound healing requires further investigation. Plasma and B cells also increase during the inflammatory phase and peak during the proliferative phase, which has been shown to support wound healing (Figures 4H and 4I).⁵² Conversely, cDC1 and cDC2 proportions initially decrease at the onset of inflammation but rebound as healing progresses, paralleling the reduction in neutrophils and macrophages (Figures 4C and 4D).

During the inflammatory phase of wound repair, keratinocytes began migrating rapidly, coinciding with peak activities of immune cells (Figure 4J). To explore whether immune cells communicate with keratinocytes to promote re-epithelialization, we used the MultiNicheNet R package⁵³ to analyze cell-to-cell communication. Top 50 ligand-receptor interactions influencing migrating keratinocytes were identified, which included many signals previously known to enhance keratinocyte motility, such as *THBS1*,⁵⁴ *LGALS3*,⁵⁵ and *TNF*⁵⁶ (Figure 4K; Table S5). Notably, *CXCL1* and *CXCL5*, typically involved in recruiting inflammatory cells,⁵⁷ also promoted keratinocyte migration in a *FOSL1*-dependent manner (Figures 4L, S5A, and S5B). While *CXCL1* did not alter *FOSL1* mRNA levels (Figure 4M), it triggered the phosphorylation of Ser265 in *FOSL1*'s C-terminal destabilizer region, enhancing *FOSL1* stability⁵⁸ (Figures 4N, 4O, and S5C). This effect was reversed by the ERK pathway inhibitor U0126, highlighting the role of ERK signaling in this regulatory process (Figure 4O).

Furthermore, CellChat⁵⁹ was used to compare cell-to-cell communication between skin and wounds, identifying EGFR signaling as a wound-specific pathway influencing both Bas-mig and Spi-mig (Figures 4P, S5D, and S5E). Intriguingly, while epidermal growth factor (EGF) receptors (*EGFR* and *ERBB2*) were highly expressed on keratinocytes and FBs, the expected EGF ligand was absent in our scRNA-seq and ST-seq data, questioning its assumed role in wound healing. Instead, ligands such as *TGFA*, *AREG*, and *HB-EGF* were rapidly upregulated in migrating keratinocytes, likely serving as autocrine signals during the inflammatory phase, whereas *EREG* was predominantly expressed by wound macrophages (Figure 4P). These EGFR ligands significantly enhanced keratinocyte migration and induced mRNA expression of *FOSL1*, a key regulator of keratinocyte motility (Figures 4L, 4M, and S5A).

Considering cellular sources of these pro-migratory signals, we analyzed the spatial co-occurrence of cell types in ST-seq, noting that cell-to-cell communication, particularly juxtacrine and paracrine signaling, was spatially restricted. In niches with migrating keratinocytes (niches 7 and 8), we observed their close associations with pro-inflammatory macrophages and plasma cells at the wound edge (Figures 1F and S2F), further confirmed by IF staining (Figure 6C).

Our study thus outlines a detailed framework for understanding cell-to-cell communication signals directing re-epithelialization: in the early inflammatory phase, keratinocytes generate autocrine EGF signals (*TGFA*, *AREG*, and *HBEGF*), while nearby pro-inflammatory macrophages contribute paracrine EGF (*EREG*) and chemokine signals (*CXCL1* and *CXCL5*), collaboratively enhancing *FOSL1* expression at both mRNA and protein levels and promoting keratinocyte migration.

FBs play a major role in promoting re-epithelialization at the proliferative phase

Our scRNA-seq identified four main FB clusters consistent with previous studies^{9,60}: mesenchymal (FB-I: *POSTN*⁺), pro-inflammatory (FB-II: *C3*⁺), papillary (FB-III: *ELN*⁺*LEPR*⁺), and proliferating (FB-prolif: *MKI67*⁺) FBs (Figures 5A–5C and S5F; Table S4). FB-I was subdivided into four subclusters with distinct markers (*COL11A1*⁺, *MMP11*⁺, *COL4A1*⁺, and *SFRP4*⁺*COMP*⁺), while FB-II was split into two subclusters differentiated by apolipoproteins (*APOD*⁺ or *APOE*⁺) and immune genes (*ITM2A*⁺ or *CCL19*⁺). Two additional FB clusters were identified: one adjacent to hair follicles (*SFRP1*⁺*CRABP1*⁺) and another similar to papillary FBs (*ELN*⁺*SFRP4*⁺), as shown in ST-seq deconvolution and dendrogram analysis, respectively (Figures 5C and S5G). RNA velocity analysis⁶¹ depicted two FB trajectories: one from FB-I (*SFRP4*⁺*COMP*⁺) to FB-II (*APOE*⁺*CCL19*⁺) and another from FB-I (*POSTN*⁺*COL11A1*⁺) to FB-III (*ELN*⁺*LEPR*⁺) (Figure S5H). Cells in the initial state of the first trajectory highly expressed PI16, a progenitor FB marker⁶² (Figure S5I). Cellular proportion and Milo analysis showed that proliferating FBs were specifically present during the proliferative phase (Wound7), mesenchymal FBs (FB-I) increased and dominated the wound bed in the remodeling phase (Wound30), and pro-inflammatory (FB-II) and papillary (FB-III) FBs declined as healing progressed (Figures 5D, 5E, and S5J). These shifts in FB heterogeneity were validated by ST-seq deconvolution and further confirmed by FISH (Figures 5F and 5G).

Upon comparing signals influencing keratinocyte migration across the inflammatory and proliferative phases, we noted a

(F) UMAP of lymphoid subpopulations.

(G) Dot plot of marker gene expression in lymphoid clusters.

(H) Cell proportions of lymphoid cell types.

(I) Milo beeswarm plot showing the differential abundance of cell types between Wound1 and skin.

(J) The dynamics of immune cells and migrating keratinocytes during wound healing.

(K–M) (K) Circos plot showing top 50 cell-cell interactions between cell types (ligand) and migrating keratinocytes (receptor) in Wound1. Cell migration assay (L) and *FOSL1* mRNA expression (M) in primary human keratinocytes treated with growth factors or cytokines.

(N) Western blot of *FOSL1* protein in keratinocytes treated with *CXCL1* for 4 and 8 h.

(O) Western blot of phosphorylated and total ERK and *FOSL1* proteins in keratinocytes treated with *CXCL1* for 30 min, with or without ERK pathway inhibitor U0126. GAPDH was used as a loading control.

(P) Violin plot showing EGF signaling ligand and receptor expression in each cell type. Significances were determined using generalized linear modeling on a quasi-binomial distribution (C and H), one-way ANOVA test (L and M), and Mann-Whitney U test (P), comparing other conditions with normal skin/control group, **p* < 0.05, ***p* < 0.01, ****p* < 0.001.

See also Tables S4 and S5.

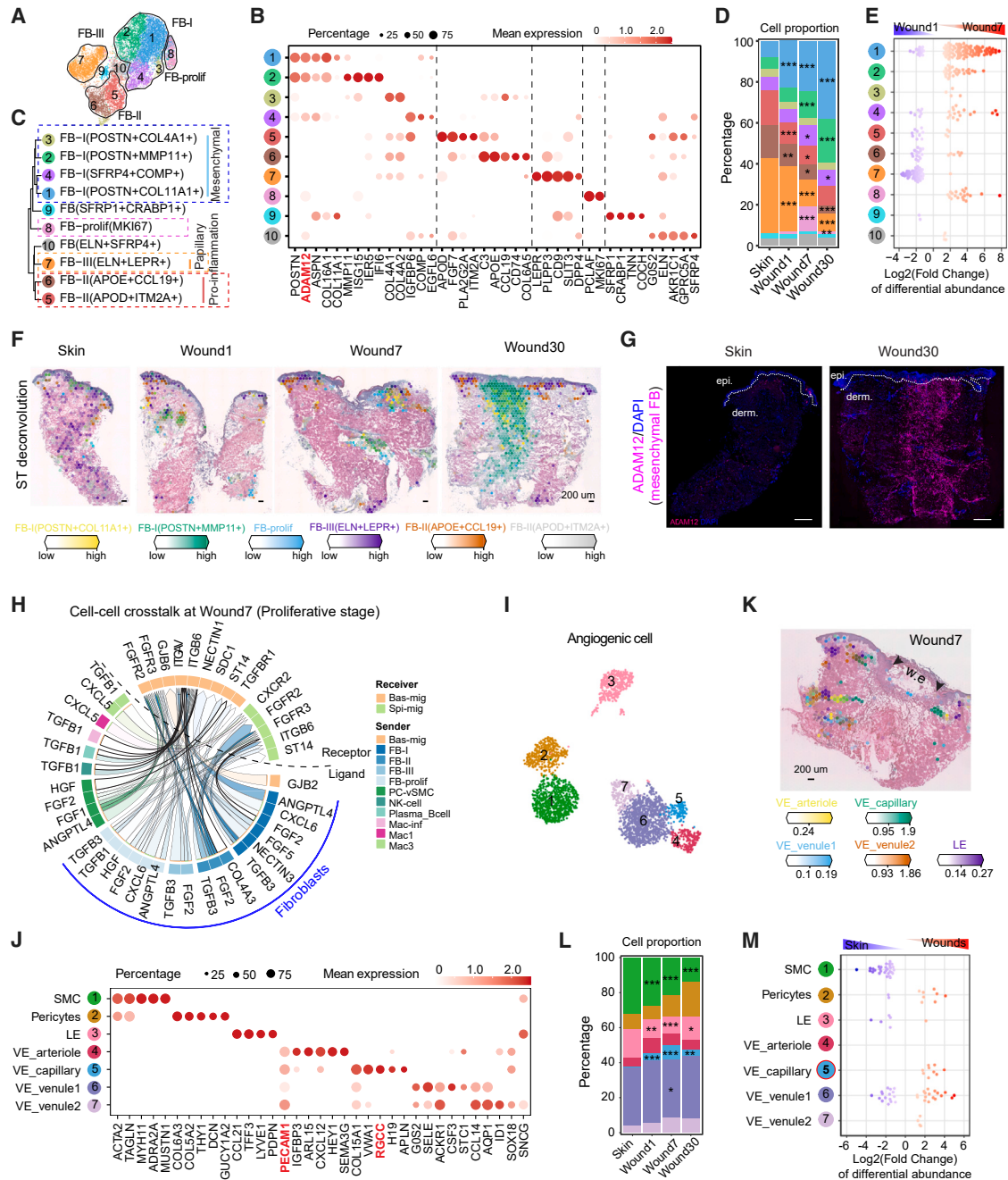


Figure 5. Fibroblasts play a major role in promoting re-epithelialization at the proliferative phase

- (A) UMAP of fibroblast subpopulations.
 (B) Dot plot of marker gene expression in clusters.
 (C) Dendrogram illustrating cell clusters' relatedness based on gene expression.
 (D) Cell proportions of FB clusters.
 (E) Milo beeswarm plot showing the differential abundance of cell types between Wound7 and Wound1. Blue and red dots indicate significantly decreased and increased cell abundance, respectively.
 (F) Deconvolution of fibroblast subpopulations in ST-seq. Donor 2 is shown.
 (G) FISH images of *ADAM12* expression (marker of mesenchymal FB) in skin and Wound30. Scale bar, 500 μ m.
 (H) Circos plot of top 50 cell-cell interactions between cell types (ligand) and migrating keratinocytes (receptor) in Wound7.
 (I) UMAP of angiogenic subpopulations.
 (J) Dot plot of marker gene expression in clusters.
 (K) Deconvolution of endothelial populations in Wound7 ST-seq. Donor 1 is shown.

(legend continued on next page)

shift from macrophages as primary influencers during the inflammatory phase to FBs playing a pivotal role in the proliferative phase (Figures 4K and 5H). Proliferating FBs increased the production of growth factors such as *HGF*, *FGF2*, and *TGF β 1* during the proliferative phase, boosting keratinocyte motility^{63–65} (Figures 5H and 4L; Table S5). HGF also upregulated FOSL1 expression in keratinocytes, a critical factor in cell motility (Figure 4M; Table S5). Additionally, ST-seq revealed close associations between FB-prolif and Bas-mig (niche 7), as well as inflammatory macrophages (niche 13) at the wound edge, highlighting FBs' role in re-epithelialization (Figures 1F and S2F). Thus, our findings suggest that pro-inflammatory macrophages and FBs sequentially support keratinocyte migration during different healing stages, functioning like a relay race.

Macrophage interactions with FBs and endothelial cells during wound healing

Our scRNA-seq analysis identified seven angiogenic cell types in human acute wounds, including various endothelial cells (lymphatic, arteriole, and capillary) and two venule endothelial subsets, along with associated smooth muscle cells and pericytes (Figures 5I and 5J; Table S4). Deconvolution of ST-seq highlighted well-defined vascular structures formed by these cells in the dermis (Figures 5K, S5K, and S5L). Post-injury, cellular proportion and Milo analysis showed a decrease in smooth muscle cells and lymphatic endothelial populations, while capillary endothelial cells notably increased during the proliferative phase, indicating active angiogenesis (Figures 5L and 5M). Additionally, ST-seq revealed close associations between capillary endothelial cells, proliferating FBs, and pro-inflammatory macrophages (niche 13) during the proliferative phase, characterizing the newly formed granulation tissue (Figures 1F and S2F).

During wound healing, macrophages interact with FB and vascular endothelial cells (VE) at different stages.⁴⁶ Cell-cell crosstalk reveals that inflammatory macrophages dominate the early stages (Wound1), while pro-resolution macrophages become more active in later phases (Wound7, Wound30) (Figures S5M and S5N). In Wound1, inflammatory macrophages release *CCL7* and *IL1A/B*, targeting VE and FB, respectively. *CCL7* activates inflammatory pathways, increasing vascular permeability and immune cell infiltration,^{66,67} while *IL1A/B* promotes FB proliferation, migration, and collagen and MMP production.⁶⁸ By day 7, *TGF- β* from Mac_inf and Mac3 act on VE, and *C1QB* from Mac2 influences FB, promoting FB proliferation, collagen synthesis, and angiogenesis.^{69–71} In Wound30, *IGF-1* from Mac2 targets VE and FB, while *ITGB2* and *C1QB* from Mac2 and Mac_inf interact with FB, enhancing angiogenesis, FB activation, myofibroblast differentiation, and wound strength.^{72,73} Therefore, pro-inflammatory and pro-resolution macrophages play key roles in wound repair by interacting with keratinocytes, FBs, and endothelial cells.

Multi-facet pathological changes in chronic wounds

To advance our research on chronic wound pathology, we integrated scRNA-seq data from acute human wounds with VUs and DFU data²⁸ (Figure 1G). We identified distinct pathological changes between chronic wound types, differing by prognosis and etiology.

We found significant reductions in migratory keratinocytes in DFUs and their complete absence in VUs, correlating with re-epithelialization failure in chronic wounds^{3,74} (Figure 6A). Consistent with this, scRNA-seq data revealed fewer FOSL1⁺ keratinocytes in both DFUs and VUs compared with acute wounds, a trend more evident at the protein level as shown by IF analysis (Figures 6B and 6C). In a mouse model, increased FOSL1 expression was observed at the wound edges of normal mice but not in diabetic (db/db) mice, indicating that FOSL1 deficiency hinders re-epithelialization (Figure 6D). Unlike acute wounds, where keratinocyte proliferation increases, non-healing DFUs show reduced keratinocyte proliferation, while VUs display highly proliferative keratinocytes at wound edges, consistent with the hyperproliferative epidermis observed in VU edges⁷⁵ (Figures S3C and S6A).

In human chronic wounds, we also analyzed cell-to-cell signals crucial for re-epithelialization, including *CXCL1*, *EGFR* ligands, and *HGF*. Analysis using single-cell data (Theocharidis et al.⁷ and ours), bulk RNA-seq (GSE174661¹²), and microarray data (GSE80178⁷⁶) showed that *CXCL1* was upregulated in VUs, similar to acute wounds, but not in DFUs (Figures 6E–6G). RT-qPCR confirmed these results, indicating higher *CXCL1* levels in VUs and lower in DFUs (Figure 6H). Additionally, scRNA-seq data demonstrated abundant *EGF* ligands and receptors expression in acute wounds, but this was reduced or weakly induced in non-healing DFU and VU compared with normal skin (Figure 6I). *HGF* and its receptor *MET* also displayed low expression in DFUs, while in VUs, their levels were similar to those in acute wounds (Figure 6I). Therefore, lacking FOSL1⁺ migrating keratinocytes in VUs may be linked to inadequate *EGF* signaling, while diminished *CXCL1*, *EGF*, and *HGF* signals may collectively hinder healing in DFUs.

Our research highlights the critical role of inflammation in tissue repair.⁷⁷ In contrast to the significant increase of pro-inflammatory Mac, DC3, plasma cells, and Th cells in acute wounds, these cells were notably scarce in DFUs and VUs. Specifically, VUs exhibited a marked deficiency in pro-inflammatory macrophages (Figures 6J, 6K, and S6B). Although DFUs maintained similar proportions of Mac_inf and Mac1 as acute wounds, their macrophages displayed a significant reduction in gene expression crucial for cellular functions,⁴⁶ such as cytokine signaling (*CXCL1*, *CXCL5*, and *CCL20*), lipopolysaccharide (LPS) response, and oxidative stress (Figure 6L). These findings suggest an impaired inflammatory response in chronic wounds, which may revise the conventional view of sustained inflammation in these conditions.^{78,79}

Furthermore, we observed a notable absence of proliferating and mesenchymal FBs in chronic wounds, suggesting a

(L) Cell proportions of angiogenic clusters.

(M) Milo beeswarm plot showing the differential abundance of cell types between wounds and skin. Significance was assessed using generalized linear modeling on a quasi-binomial distribution (D and L), comparing other conditions to normal skin, * $p < 0.05$, ** $p < 0.01$, *** $p < 0.001$. See also Tables S4 and S5.

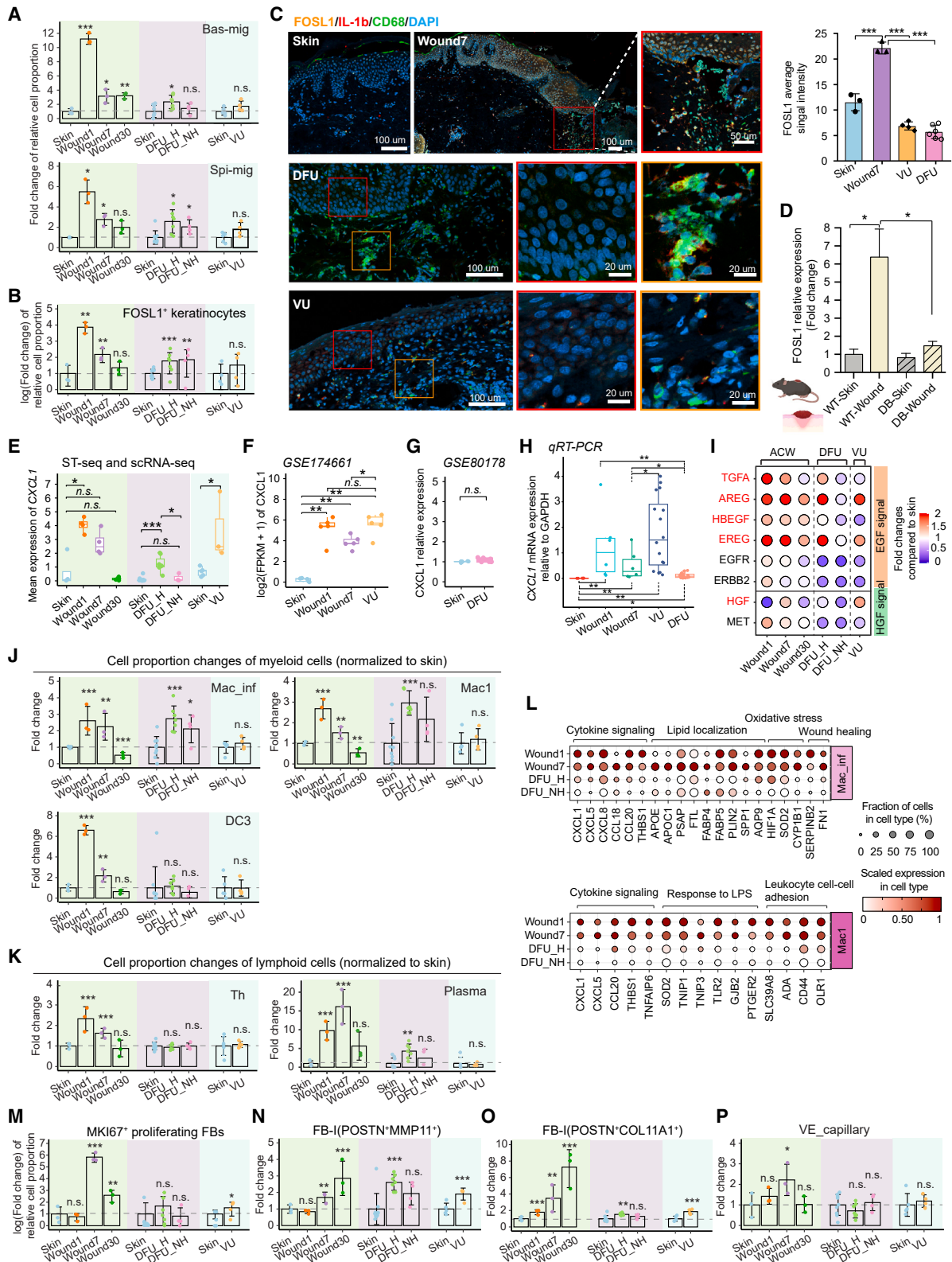


Figure 6. Multi-facet pathological changes in chronic wounds

(A) Cell proportions of Bas-mig (upper) and Spi-mig (lower) in acute and chronic wounds. DFU_H/_NH, healed/non-healed diabetic foot ulcers; VU, venous ulcer. (B) Bar charts of FOSL1⁺ cell proportion in total keratinocytes normalized to skin. The fold changes (FCs) or logFC of cell proportions normalized to their skin were used in comparisons.

(legend continued on next page)

deficiency in FB proliferation and a reduced mesenchymal stem cell response^{80,81} (Figures 6M–6O). Neither DFUs nor VUs exhibited the expected increase in VE_capillary cells characteristic of the proliferative phase of acute wounds, suggesting impeded angiogenesis, in line with previous studies⁸² (Figure 6P). Specifically, VUs displayed increased venule endothelial cells, reflecting the vascular abnormalities associated with chronic venous insufficiency⁸³ (Figure S6C).

Taken together, we identified critical pathological changes in chronic wounds compared with acute wounds, including compromised re-epithelialization, altered inflammatory responses, impaired granulation tissue formation, and hindered angiogenesis. Notably, DFUs with better healing outcomes displayed less severe pathological changes, characterized by increased presence of Bas-mig keratinocytes, inflammatory macrophages, mesenchymal FBs, and enhanced *CXCL1*, *EGF*, and *HGF* signaling, highlighting the critical role of these processes in wound healing.

Comparison of human and murine skin wound healing

While studying cellular heterogeneity in skin wounds of mouse models has enhanced our understanding of wound healing dynamics,^{23,84–87} human wound healing mechanisms differ significantly due to variations in skin structure and healing processes.⁸⁸ To bridge this gap, we compared human and mouse wounds by integrating scRNA-seq data from both species.¹⁸ We first compared our human Wound1 data with mouse acute wounds at 3 days post-injury (Figures 7A and S7A), followed by a broader comparison between our human time-course data and a mouse scRNA-seq dataset at 2, 4, and 7 days post-injury (PWD2, 4, 7)⁸⁹ to better understand cross-species wound healing dynamics (Figures S7C and S7D). We identified similar cell types across species, such as migrating keratinocytes with shared markers like *NRG1*, *IL24*, *FOSL1*, *AREG*, and *GJB2*, suggesting a conserved regulatory mechanism for keratinocyte migration (Figures 7A–7C, S7D, and S7E; Table S6). We have validated that *FOSL1* was highly expressed in wound-edge migrating keratinocytes in both human and mouse acute wounds by IF staining (Figures 3L and S3K). Notably, recent research has shown that IL-24, upregulated in epithelial stem cells, promotes wound repair by enhancing re-epithelialization, vascular regeneration, and FB activation, acting independently of microbial and adaptive immune factors.⁹⁰

Our scRNA-seq data reveal key structural differences between murine and human skin: humans have a thicker epidermis with more spinous keratinocytes (integrated clusters 4–6), mice possess abundant hair follicles (clusters 7 and 8), and a unique

panniculus carnosus structure (cluster 11 *MYF6/Mrf4*)⁹¹ (Figures 7A, S7B, and S7D). These structural variances affect wound healing mechanisms: mice primarily heal through panniculus carnosus contraction, whereas humans rely on re-epithelialization and granulation tissue formation.⁹² Additionally, human wounds show a higher presence of mast cells (cluster 17), aligning with findings of greater mast cell heterogeneity in humans than in mice⁹³ (Figures 7A and S7D). Murine wounds also have more proliferating cells at the G2/M phase of the cell cycle, consistent with their more robust healing capabilities (Figures 7D and S7F).

Beyond cellular composition, gene expression differences between mice and humans were even more striking (Figure 7E; Table S6). For instance, migration-related genes such as *MMP1*, *S100A2/7/8/9*, and *SERPINB3/4* are highly expressed in humans but barely in mice (Figures 7E, 7F, S7G, and S7I). *MMP1* supports human keratinocyte migration by breaking down dermal collagen, a role filled by *MMP13* in mice, indicating species-specific proteolysis mechanisms for re-epithelialization.^{94,95} *S100A* proteins contribute to antimicrobial defense and tissue repair,⁹⁶ while *SERPINB3/4* play a crucial role in keratinocyte inflammatory responses.⁹⁷ The distinct gene expressions likely reflect differing adaptations to microbial threats. Further, GO analysis of DEGs showed that human migrating keratinocytes are enriched with genes related to mitochondrial activity, which support wound healing functions such as energy provision and inflammation regulation⁹⁸ (Figure 7G; Table S6). In contrast, murine migrating keratinocytes show a proliferation-focused gene expression, supporting their dual role in cell proliferation and migration, as validated by *FOSL1/MKI67* co-staining in murine wounds (Figures 7G, S3G, and S3K).^{33,34}

Temporal changes in cell-type proportions during wound repair in humans and mice show increases in proliferating keratinocytes and FBs, migrating keratinocytes, plasma/B cells, monocytes/macrophages, and neutrophils in acute wounds (Figure S7H).

However, mesenchymal FBs (FB_I) increase over time in humans but decrease in mice, while T cells rise early in human wounds and decline in mice during the initial healing stage.

Additionally, cell-to-cell communication during wound healing differs between species. In human wounds, *EGFR* ligands are produced by macrophages, dendritic cells, endothelial cells, and migrating keratinocytes (Figure 4P), while in mouse wounds, they are mainly expressed by keratinocytes and FBs, not immune cells.⁹⁹ IF analysis confirmed that EREG, an *EGFR* ligand, is produced by both macrophages and keratinocytes in human wounds, but primarily by keratinocytes in mouse wounds

(C) Immunofluorescence staining of *FOSL1* (migrating keratinocyte marker), *IL1b*, and *CD68* (pro-inflammatory macrophage markers) in human skin, acute, and chronic wounds. DAPI stains the nuclei. Scale bars: 100 μ m in low-magnification images and 20 μ m in high-magnification images. The signal intensity of epidermal *FOSL1* was quantified.

(D–G) (D) Relative gene expression of *Fos1* in the epidermis of wild-type (WT) and diabetic (DB) mouse skin and wounds. $n = 5$. Boxplots showing *CXCL1* expression in our ST-seq (acute wounds) and scRNA-seq (DFU and VU) datasets (E), public bulk RNA-seq data of skin and acute wounds from 5 donors and 5 VUs (F), and microarray data of skin ($n = 6$) and DFU ($n = 6$) (G).

(H) RT-qPCR of *CXCL1* in human acute wounds from 7 donors, 16 VUs, and 27 DFUs.

(I–P) (I) Dot plot showing the fold changes of ligands and receptors of *EGF* and *HGF* signals in acute and chronic wounds normalized to the control skin. Cell proportions of myeloid cells (J), lymphoid cells (K), proliferating FB (M), FB-I(*POSTN*⁺*MMP11*⁺) (N), FB-I(*POSTN*⁺*COL11A1*⁺) (O), and VE-capillary (P) in acute and chronic wounds. (L) Dot plots showing scaled expression of DEGs between acute wounds and DFU in *Mac_inf* (upper) and *Mac1* (lower).

Genes enriched in relevant GO terms were plotted. Significances were assessed using generalized linear modeling on a quasi-binomial distribution (A, B, J, K, M–P), one-way ANOVA test (C and D), and Mann-Whitney U test (E–H), * $p < 0.05$, ** $p < 0.01$, *** $p < 0.001$, n.s.: no significance.

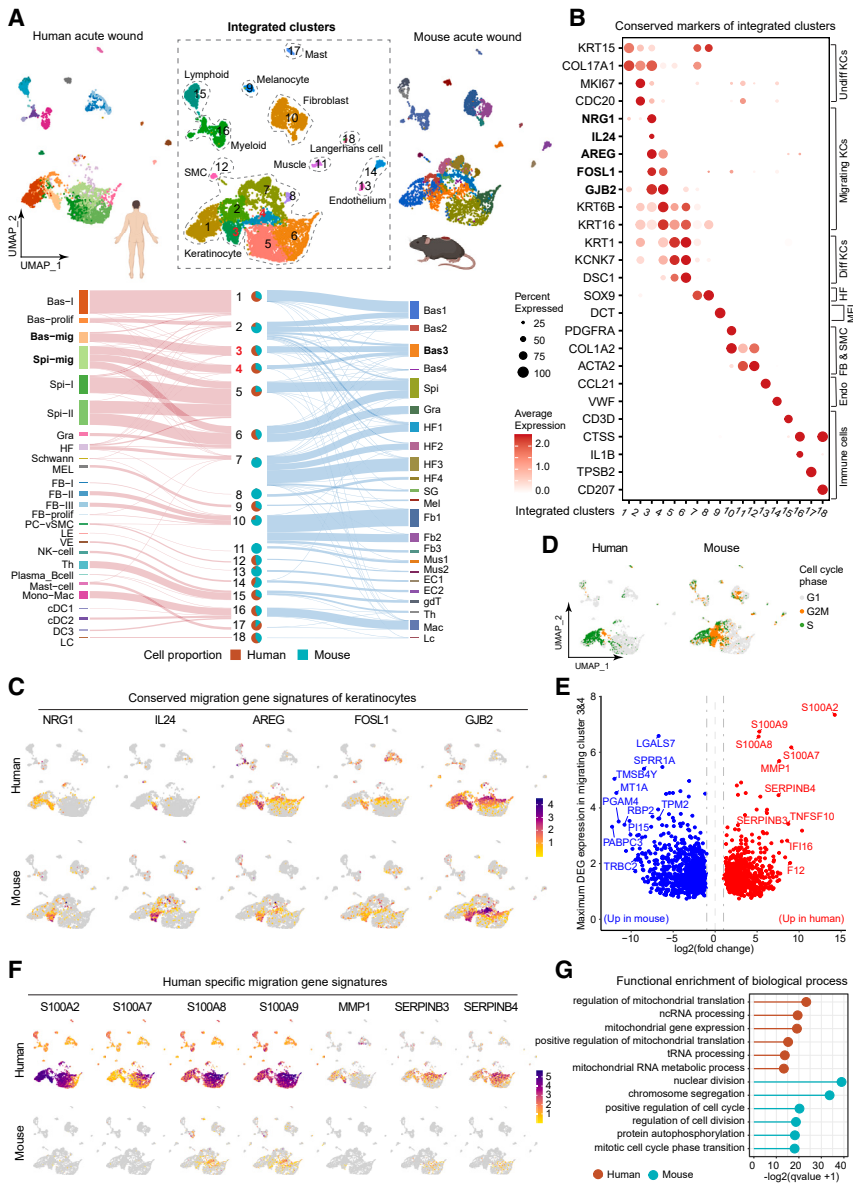


Figure 7. Comparison of human and murine skin wound healing

(A) UMAP of integrated cell clusters from human and mouse acute wounds. The top-left and top-right plots show color-coded human and mouse cell types separately. The Sankey diagram traces the cellular assignments of integrated clusters from the original human and mouse cell types, and the pie chart reveals their contributions to each cluster. SG, sweat gland cell; Mus, muscle cell; EC, endothelial cell; gdT, gamma-delta T cell.

(B) Dot plot of conserved marker gene expression of integrated clusters. Undiff/Diff, undifferentiated/differentiated KC; Endo, endothelium.

(C) Feature plots showing representative conserved gene signatures of migrating keratinocytes.

(D) Cell cycle analysis in human and mouse wound cells.

(E) Volcano plot showing DEGs in migrating keratinocytes (clusters 3 and 4) between human and mouse wounds. Red and blue dots represent up-regulated genes in humans and mice, respectively. The top 10 changed genes are highlighted.

(F) Feature plots showing representative human-specific migration gene signatures.

(G) Lollipop chart showing enriched GO terms of human- and mouse-DEGs in (E).

See also Table S6.

DISCUSSION

Wound healing involves intricate coordination of various cell types and molecular signals, which have been primarily studied in animal and *in vitro* models. To better understand how these mechanisms apply to humans, we utilized single-cell and spatial transcriptomics in a unique *in vivo* human wound-healing model. This innovative approach allows us to trace the healing process's dynamics and cellular changes with unprecedented precision and consistency across an individual's recovery. With this spatiotemporal cell atlas of human skin wound healing, we delve into re-

epithelialization, illuminating the cellular architecture of the human wound tongue, its gene regulatory networks, and the cell-to-cell communication that promotes keratinocyte motility. The study also highlights cellular and molecular discrepancies in chronic wounds and identifies potential therapeutic targets. This pivotal dataset is a vital resource for validating the relevance of animal model findings and stimulates further research into human wound healing mechanisms. To facilitate global research collaboration and drive further discoveries, we have made this groundbreaking roadmap of human skin wound healing accessible for interactive exploration online (<https://www.xuandenlab.com/tools>).

Cell-to-cell communication signals are promising therapeutic targets for enhancing tissue repair. Our study on human wounds challenges established paradigms, particularly in ligand-receptor signaling. Keratinocytes are pivotal in initiating immune responses

epithelialization, illuminating the cellular architecture of the human wound tongue, its gene regulatory networks, and the cell-to-cell communication that promotes keratinocyte motility. The study also highlights cellular and molecular discrepancies in chronic wounds and identifies potential therapeutic targets. This pivotal dataset is a vital resource for validating the relevance of animal model findings and stimulates further research into human wound healing mechanisms. To facilitate global research collaboration and drive further discoveries, we have made this groundbreaking roadmap of human skin wound healing accessible for interactive exploration online (<https://www.xuandenlab.com/tools>).

Cell-to-cell communication signals are promising therapeutic targets for enhancing tissue repair. Our study on human wounds challenges established paradigms, particularly in ligand-receptor signaling. Keratinocytes are pivotal in initiating immune responses

through cytokines, chemokines, and growth factors, and their activity varies with the stimulus and context.¹⁰² We identified *IL18*, *CCL27*, and *CXCL14* as the primary cytokines/chemokines produced by keratinocytes in acute human wounds (Figure S7L). *IL-18* is critical in starting inflammation during bacterial infections,¹⁰³ *CCL27* aids T cell-mediated inflammation¹⁰³ and skin regeneration,¹⁰⁴ and *CXCL14* recruits immune cells, inhibits angiogenesis, and has antimicrobial properties.^{105,106} Despite their significant roles, these cytokines are often overlooked in wound repair studies. Additionally, some cytokines are produced by specific keratinocyte clusters (Figure S7L). For example, basal migrating keratinocytes express *IL-20* and *IL-24*, targeting the *IL-22R* receptor; granular keratinocytes produce *IL36G* and *IL36RN*, supporting wound healing.^{107,108} Furthermore, our findings reveal that, while *IL1A/B/RN*, *IL6*, and *CXCL1/5/8* are commonly associated with keratinocytes *in vitro*, in human wounds *in vivo*, these cytokines and chemokines are primarily produced by macrophages, dendritic cells, and FBs, not by keratinocytes (Figure S7L). This insight challenges previous assumptions based on *in vitro* studies and highlights the complexity of cellular interactions in actual wound environments.

Many molecular signals have been previously reported to regulate keratinocyte motility, and our study evaluated the physiological relevance of these signals in human skin wound repair. During the early inflammatory phase, keratinocytes initiate autocrine *EGFR* signaling, while pro-inflammatory macrophages enhance cell migration by contributing additional *EGFR* and *CXCL1* signals. Although *CXCL1* is typically associated with recruiting inflammatory cells such as neutrophils, it also plays a critical role in promoting keratinocyte migration,¹⁰⁴ and blocking its receptor, *CXCR2*, can impede re-epithelialization independently of neutrophils.¹⁰⁹ Our observations of reduced pro-inflammatory macrophage activity in chronic wounds align with the longstanding theory that inflammation is essential for tissue repair.⁷⁷ The current perspective on inflammation in chronic wounds is shifting from being viewed as persistently excessive¹¹⁰ to dysfunctional, characterized by impaired monocyte recruitment and macrophage and neutrophil dysfunction.^{111,112} Therefore, precise modulation of pathological inflammation, rather than its inhibition, may be crucial for effective chronic wound therapy.

Limitations of the study

Our study has some limitations. The Visum ST data lack single-cell resolution. Higher-resolution ST needed in future studies could shed light on the spatial arrangement of cell states at the cellular or subcellular level. Additionally, our sampling of human acute wounds at days 1, 7, and 30 post-injury captures key healing phases, but the limited time points may overlook transient cell states and ephemeral cell-to-cell interactions; hence, a higher temporal resolution would be advantageous. The anatomical diversity of skin, recognized at histological,¹¹³ functional,^{114,115} and gene expression levels,^{116,117} may influence wound healing. Therefore, the different wound locations could be a significant confounding factor in this study's comparison. Moreover, limited tissue availability and high costs of single-cell and spatial omics technologies constrained the total cell number in this study, potentially limiting the discovery of rare cell types. Given the variability of human chronic wounds,

more extensive cohort studies and cross-dataset comparisons are crucial to confirm our findings and aid in the molecular stratification of complex chronic wounds.

RESOURCE AVAILABILITY

Lead contact

Further information and requests for resources and reagents should be directed to and will be fulfilled by the lead contact, Ning Xu Landén (ning.xu@ki.se).

Materials availability

This study did not generate new, unique reagents.

Data and code availability

Data sequenced in this study have been deposited in GEO under accession numbers: GSE241132, GSE265972, GSE241124, and GSE218430. All original code for reproducible results has been deposited at GitHub with the DOI: <https://doi.org/10.5281/zenodo.14176654>. The scRNA-seq and ST-seq data can be explored at the web porter <https://www.xulandenlab.com/tools>. Any additional information required to reanalyze the data reported in this paper is available from the lead contact upon request.

ACKNOWLEDGMENTS

We thank all the healthy donors and patients who participated in this study. The computations and data handling were enabled by resources in projects of sens2020010, SNIC2022/22-873, and NAISS 2023/22-935 provided by the National Academic Infrastructure for Supercomputing in Sweden (NAISS) at UPPMAX, funded by the Swedish Research Council through grant agreement no. 2022-06725. N.X.L. was supported by Swedish Research Council (Vetenskapsrådet) grants (2020-01400), the Ragnar Söderbergs Foundation (M31/15), the Welander and Finsens Foundation (Hudfonden), the Ming Wai Lau Centre for Reparative Medicine, the LEO Foundation, Cancerfonden, the Åke Wiberg Foundation, and the Karolinska Institutet. D.L. was supported by the National Natural Science Fund for Excellent Young Scientists Fund of China, the National Natural Science Foundation of China (82272294), the Distinguished Medical Expert of Jiangsu Province, the Non-profit Central Research Institute Fund of Chinese Academy of Medical Sciences (2022-RC320-02, 2021-RC320-001, and 2020-RC320-003), the CAMS Innovation Fund for Medical Sciences (2021-I2M-1-059), and the Jiangsu Provincial Medical Key Laboratory, Jiangsu Province Capability Improvement Project through Science, Technology, and Education (ZDXYS202204). M.K. was supported by Vetenskapsrådet (2022-01059), Cancerfonden (21 1821 Pj), and LEO foundation (LF-OC-19-000225).

AUTHOR CONTRIBUTIONS

N.X.L., Z.L., and D.L. conceived and designed the study. P.S., L.G., J.G., C.C., Y.X., W.H., and L. Zhu collected clinical samples. D.L., X.B., L. Zhang, L. Li, and J.W. performed experiments. Z.L. performed bioinformatics analysis with the support from Å.K.B., L. Luo., and Y.C. D.H. and D.B.-L. made the WebAtlas tool for spatial data. M.H., M.K., C.L.B., N.H.G., and K.A. helped with data analysis and presentation. Z.L. and N.X.L. wrote the manuscript with input from all authors. All authors read and approved the final version of the manuscript.

DECLARATION OF INTERESTS

The authors declare no competing interests.

STAR★METHODS

Detailed methods are provided in the online version of this paper and include the following:

- KEY RESOURCES TABLE
- EXPERIMENTAL MODEL AND STUDY PARTICIPANT DETAILS

- Human wound sample collection
- Mice wound sample collection
- **METHOD DETAILS**
 - Human and mouse single-cell RNA sequencing
 - Spatial transcriptomic sequencing
 - Human scRNA-seq data processing
 - Mouse single-cell sequencing data processing
 - Differential abundance testing with Milo
 - SCENIC and CellOracle analyses
 - Trajectory analysis of keratinocytes and fibroblasts
 - Gene ontology analysis
 - M1 and M2 signature
 - Cell-to-cell communication analysis
 - ST-seq data processing
 - Pseudobulk analysis of scRNA-seq and ST-seq
 - Deconvolution of ST-seq data and wound bulk RNA-seq data
 - Venous ulcer scRNA-seq analysis
 - Integration of wounded skin scRNA-seq datasets
 - Cross-species comparison of human and mouse wound healing
 - Fluorescent *in situ* hybridization (FISH)
 - Immunofluorescence staining and microscopy
 - RNA extraction and qRT-PCR
 - Keratinocyte culture, treatment, RNA extraction, and qRT-PCR
 - Cell migration assay
 - Western blotting
- **QUANTIFICATION AND STATISTICAL ANALYSIS**
 - Softwares and statistics

SUPPLEMENTAL INFORMATION

Supplemental information can be found online at <https://doi.org/10.1016/j.stem.2024.11.013>.

Received: May 25, 2024

Revised: September 24, 2024

Accepted: November 22, 2024

Published: December 26, 2024

REFERENCES

1. Cañedo-Dorantes, L., and Cañedo-Ayala, M. (2019). Skin Acute Wound Healing: A Comprehensive Review. *Int. J. Inflam.* *2019*, 3706315. <https://doi.org/10.1155/2019/3706315>.
2. Peña, O.A., and Martin, P. (2024). Cellular and molecular mechanisms of skin wound healing. *Nat. Rev. Mol. Cell Biol.* *25*, 599–616. <https://doi.org/10.1038/s41580-024-00715-1>.
3. Pastar, I., Stojadinovic, O., Yin, N.C., Ramirez, H., Nusbaum, A.G., Sawaya, A., Patel, S.B., Khalid, L., Isseroff, R.R., and Tomic-Canic, M. (2014). Epithelialization in Wound Healing: A Comprehensive Review. *Adv. Wound Care (New Rochelle)* *3*, 445–464. <https://doi.org/10.1089/wound.2013.0473>.
4. Darwin, E., and Tomic-Canic, M. (2018). Healing Chronic Wounds: Current Challenges and Potential Solutions. *Curr. Dermatol. Rep.* *7*, 296–302. <https://doi.org/10.1007/s13671-018-0239-4>.
5. Pastar, I., Wong, L.L., Egger, A.N., and Tomic-Canic, M. (2018). Descriptive vs mechanistic scientific approach to study wound healing and its inhibition: is there a value of translational research involving human subjects? *Exp. Dermatol.* *27*, 551–562. <https://doi.org/10.1111/exd.13663>.
6. Li, D., Cheng, S., Pei, Y., Sommar, P., Kärner, J., Herter, E.K., Toma, M.A., Zhang, L., Pham, K., Cheung, Y.T., et al. (2022). Single-Cell Analysis Reveals Major Histocompatibility Complex II–Expressing Keratinocytes in Pressure Ulcers with Worse Healing Outcomes. *J. Invest. Dermatol.* *142*, 705–716. <https://doi.org/10.1016/j.jid.2021.07.176>.
7. Theocharidis, G., Thomas, B.E., Sarkar, D., Mumme, H.L., Pilcher, W.J.R., Dwivedi, B., Sandoval-Schaefer, T., Sîrbulescu, R.F., Kafanas, A., Mezghani, I., et al. (2022). Single cell transcriptomic landscape of diabetic foot ulcers. *Nat. Commun.* *13*, 181. <https://doi.org/10.1038/s41467-021-27801-8>.
8. Januszzyk, M., Chen, K., Henn, D., Foster, D.S., Borrelli, M.R., Bonham, C.A., Sivaraj, D., Wagh, D., Longaker, M.T., Wan, D.C., and Gurtner, G.C. (2020). Characterization of Diabetic and Non-Diabetic Foot Ulcers Using Single-Cell RNA-Sequencing. *Micromachines (Basel)* *11*, 815. <https://doi.org/10.3390/mi11090815>.
9. Deng, C.-C., Hu, Y.-F., Zhu, D.-H., Cheng, Q., Gu, J.-J., Feng, Q.-L., Zhang, L.-X., Xu, Y.-P., Wang, D., Rong, Z., and Yang, B. (2021). Single-cell RNA-seq reveals fibroblast heterogeneity and increased mesenchymal fibroblasts in human fibrotic skin diseases. *Nat. Commun.* *12*, 3709. <https://doi.org/10.1038/s41467-021-24110-y>.
10. Liu, X., Chen, W., Zeng, Q., Ma, B., Li, Z., Meng, T., Chen, J., Yu, N., Zhou, Z., and Long, X. (2022). Single-Cell RNA-Sequencing Reveals Lineage-Specific Regulatory Changes of Fibroblasts and Vascular Endothelial Cells in Keloids. *J. Invest. Dermatol.* *142*, 124–135.e11. <https://doi.org/10.1016/j.jid.2021.06.010>.
11. Shim, J., Oh, S.J., Yeo, E., Park, J.H., Bae, J.H., Kim, S.-H., Lee, D., and Lee, J.H. (2022). Integrated Analysis of Single-Cell and Spatial Transcriptomics in Keloids: Highlights on Fibrovascular Interactions in Keloid Pathogenesis. *J. Invest. Dermatol.* *142*, 2128–2139.e11. <https://doi.org/10.1016/j.jid.2022.01.017>.
12. Liu, Z., Zhang, L., Toma, M.A., Li, D., Bian, X., Pastar, I., Tomic-Canic, M., Sommar, P., and Xu Landén, N. (2022). Integrative small and long RNA omics analysis of human healing and nonhealing wounds discovers co-operating microRNAs as therapeutic targets. *eLife* *11*, e80322. <https://doi.org/10.7554/eLife.80322>.
13. Iglesias-Bartolome, R., Uchiyama, A., Molinolo, A.A., Abusleme, L., Brooks, S.R., Callejas-Valera, J.L., Edwards, D., Doci, C., Asselin-Labat, M.L., Onaitis, M.W., et al. (2018). Transcriptional signature primes human oral mucosa for rapid wound healing. *Sci. Transl. Med.* *10*, eaap8798. <https://doi.org/10.1126/scitranslmed.aap8798>.
14. Leonardo, T.R., Chen, L., Schrementi, M.E., Shi, J., Marucha, P.T., Glass, K., and DiPietro, L.A. (2023). Transcriptional changes in human palate and skin healing. *Wound Repair Regen.* *31*, 156–170. <https://doi.org/10.1111/wrr.13068>.
15. Chen, L., Arbieva, Z.H., Guo, S., Marucha, P.T., Mustoe, T.A., and DiPietro, L.A. (2010). Positional differences in the wound transcriptome of skin and oral mucosa. *BMC Genomics* *11*, 471. <https://doi.org/10.1186/1471-2164-11-471>.
16. Wolock, S.L., Lopez, R., and Klein, A.M. (2019). Scrublet: Computational Identification of Cell Doublets in Single-Cell Transcriptomic Data. *Cell Syst.* *8*, 281–291.e9. <https://doi.org/10.1016/j.cels.2018.11.005>.
17. McGinnis, C.S., Murrow, L.M., and Gartner, Z.J. (2019). DoubletFinder: Doublet Detection in Single-Cell RNA Sequencing Data Using Artificial Nearest Neighbors. *Cell Syst.* *8*, 329–337.e4. <https://doi.org/10.1016/j.cels.2019.03.003>.
18. Hao, Y., Hao, S., Andersen-Nissen, E., Mauck, W.M., 3rd, Zheng, S., Butler, A., Lee, M.J., Wilk, A.J., Darby, C., Zager, M., et al. (2021). Integrated analysis of multimodal single-cell data. *Cell* *184*, 3573–3587.e29. <https://doi.org/10.1016/j.cell.2021.04.048>.
19. Ji, A.L., Rubin, A.J., Thrane, K., Jiang, S., Reynolds, D.L., Meyers, R.M., Guo, M.G., George, B.M., Mollbrink, A., Bergenstråhle, J., et al. (2020). Multimodal Analysis of Composition and Spatial Architecture in Human Squamous Cell Carcinoma. *Cell* *182*, 497–514.e22. <https://doi.org/10.1016/j.cell.2020.05.039>.
20. Reynolds, G., Vegh, P., Fletcher, J., Poyner, E.F.M., Stephenson, E., Goh, I., Botting, R.A., Huang, N., Olabi, B., Dubois, A., et al. (2021). Developmental cell programs are co-opted in inflammatory skin disease. *Science* *371*, eaba6500. <https://doi.org/10.1126/science.aba6500>.
21. Joost, S., Annusver, K., Jacob, T., Sun, X., Dalessandri, T., Sivan, U., Sequeira, I., Sandberg, R., and Kasper, M. (2020). The Molecular Anatomy of Mouse Skin during Hair Growth and Rest. *Cell Stem Cell* *26*, 441–457.e7. <https://doi.org/10.1016/j.stem.2020.01.012>.

22. Gonzales, K.A.U., Polak, L., Matos, I., Tierney, M.T., Gola, A., Wong, E., Infarinato, N.R., Nikolova, M., Luo, S., Liu, S., et al. (2021). Stem cells expand potency and alter tissue fitness by accumulating diverse epigenetic memories. *Science* 374, eabh2444. <https://doi.org/10.1126/science.abh2444>.
23. Guerrero-Juarez, C.F., Dedhia, P.H., Jin, S., Ruiz-Vega, R., Ma, D., Liu, Y., Yamaga, K., Shestova, O., Gay, D.L., Yang, Z., et al. (2019). Single-cell analysis reveals fibroblast heterogeneity and myeloid-derived adipocyte progenitors in murine skin wounds. *Nat. Commun.* 10, 650. <https://doi.org/10.1038/s41467-018-08247-x>.
24. Ascensión, A.M., Fuertes-Álvarez, S., Ibañez-Solé, O., Izeta, A., and Araújo-Bravo, M.J. (2021). Human Dermal Fibroblast Subpopulations Are Conserved across Single-Cell RNA Sequencing Studies. *J. Invest. Dermatol.* 141, 1735–1744.e35. <https://doi.org/10.1016/j.jid.2020.11.028>.
25. Billi, A.C., Ma, F., Plazyo, O., Gharaee-Kermani, M., Wasikowski, R., Hile, G.A., Xing, X., Yee, C.M., Rizvi, S.M., Maz, M.P., et al. (2022). Nonlesional lupus skin contributes to inflammatory education of myeloid cells and primes for cutaneous inflammation. *Sci. Transl. Med.* 14, eabn2263. <https://doi.org/10.1126/scitranslmed.abn2263>.
26. He, H., Suryawanshi, H., Morozov, P., Gay-Mimbrera, J., Del Duca, E., Kim, H.J., Kameyama, N., Estrada, Y., Der, E., Krueger, J.G., et al. (2020). Single-cell transcriptome analysis of human skin identifies novel fibroblast subpopulation and enrichment of immune subsets in atopic dermatitis. *J. Allergy Clin. Immunol.* 145, 1615–1628. <https://doi.org/10.1016/j.jaci.2020.01.042>.
27. Kleshchevnikov, V., Shmatko, A., Dann, E., Aivazidis, A., King, H.W., Li, T., Elmentaité, R., Lomakin, A., Kedlian, V., Gayoso, A., et al. (2022). Cell2location maps fine-grained cell types in spatial transcriptomics. *Nat. Biotechnol.* 40, 661–671. <https://doi.org/10.1038/s41587-021-01139-4>.
28. Korsunsky, I., Millard, N., Fan, J., Slowikowski, K., Zhang, F., Wei, K., Baglaenko, Y., Brenner, M., Loh, P.-R., and Raychaudhuri, S. (2019). Fast, sensitive and accurate integration of single-cell data with Harmony. *Nat. Methods* 16, 1289–1296. <https://doi.org/10.1038/s41592-019-0619-0>.
29. Dann, E., Henderson, N.C., Teichmann, S.A., Morgan, M.D., and Marioni, J.C. (2022). Differential abundance testing on single-cell data using k-nearest neighbor graphs. *Nat. Biotechnol.* 40, 245–253. <https://doi.org/10.1038/s41587-021-01033-z>.
30. Joost, S., Jacob, T., Sun, X., Annusver, K., La Manno, G., Sur, I., and Kasper, M. (2018). Single-Cell Transcriptomics of Traced Epidermal and Hair Follicle Stem Cells Reveals Rapid Adaptations during Wound Healing. *Cell Rep.* 25, 585–597.e7. <https://doi.org/10.1016/j.celrep.2018.09.059>.
31. Wang, F., Chen, S., Liu, H.B., Parent, C.A., and Coulombe, P.A. (2018). Keratin 6 regulates collective keratinocyte migration by altering cell-cell and cell-matrix adhesion. *J. Cell Biol.* 217, 4314–4330. <https://doi.org/10.1083/jcb.201712130>.
32. Aragona, M., Dekoninck, S., Rulands, S., Lenglez, S., Mascré, G., Simons, B.D., and Blanpain, C. (2017). Defining stem cell dynamics and migration during wound healing in mouse skin epidermis. *Nat. Commun.* 8, 14684. <https://doi.org/10.1038/ncomms14684>.
33. Park, S., Gonzalez, D.G., Guirao, B., Boucher, J.D., Cockburn, K., Marsh, E.D., Mesa, K.R., Brown, S., Rompolas, P., Haberman, A.M., et al. (2017). Tissue-scale coordination of cellular behaviour promotes epidermal wound repair in live mice. *Nat. Cell Biol.* 19, 155–163. <https://doi.org/10.1038/ncb3472>.
34. Headon, D. (2017). Reversing stratification during wound healing. *Nat. Cell Biol.* 19, 595–597. <https://doi.org/10.1038/ncb3545>.
35. Aibar, S., González-Bias, C.B., Moerman, T., Huynh-Thu, V.A., Imrichova, H., Hulselmans, G., Rambow, F., Marine, J.-C., Geurts, P., Aerts, J., et al. (2017). SCENIC: single-cell regulatory network inference and clustering. *Nat. Methods* 14, 1083–1086. <https://doi.org/10.1038/nmeth.4463>.
36. Casalino, L., Talotta, F., Cimmino, A., and Verde, P. (2022). The Fra-1/AP-1 Oncoprotein: From the "Undruggable" Transcription Factor to Therapeutic Targeting. *Cancers (Basel)* 14, 1480. <https://doi.org/10.3390/cancers14061480>.
37. Sobolev, V.V., Khashukoeva, A.Z., Evina, O.E., Geppe, N.A., Chebysheva, S.N., Korsunskaya, I.M., Tchepourina, E., and Mezentsev, A. (2022). Role of the Transcription Factor FOSL1 in Organ Development and Tumorigenesis. *Int. J. Mol. Sci.* 23, 1521. <https://doi.org/10.3390/ijms23031521>.
38. Boudra, R., and Ramsey, M.R. (2020). Understanding Transcriptional Networks Regulating Initiation of Cutaneous Wound Healing. *Yale J. Biol. Med.* 93, 161–173.
39. Kamimoto, K., Stringa, B., Hoffmann, C.M., Jindal, K., Solnica-Krezel, L., and Morris, S.A. (2023). Dissecting cell identity via network inference and in silico gene perturbation. *Nature* 614, 742–751. <https://doi.org/10.1038/s41586-022-05688-9>.
40. Adamson, S.E., Griffiths, R., Moravec, R., Senthivayagam, S., Montgomery, G., Chen, W., Han, J., Sharma, P.R., Mullins, G.R., Gorski, S.A., et al. (2016). Disabled homolog 2 controls macrophage phenotypic polarization and adipose tissue inflammation. *J. Clin. Invest.* 126, 1311–1322. <https://doi.org/10.1172/JCI79590>.
41. Wheeler, K.C., Jena, M.K., Pradhan, B.S., Nayak, N., Das, S., Hsu, C.D., Wheeler, D.S., Chen, K., and Nayak, N.R. (2018). VEGF may contribute to macrophage recruitment and M2 polarization in the decidua. *PLoS One* 13, e0191040. <https://doi.org/10.1371/journal.pone.0191040>.
42. Combes, A.J., Courau, T., Kuhn, N.F., Hu, K.H., Ray, A., Chen, W.S., Chew, N.W., Cleary, S.J., Kushnoor, D., Reeder, G.C., et al. (2021). Global absence and targeting of protective immune states in severe COVID-19. *Nature* 597, 124–130. <https://doi.org/10.1038/s41586-021-03234-7>.
43. Liu, X., Wang, Y., Lu, H., Li, J., Yan, X., Xiao, M., Hao, J., Alekseev, A., Khong, H., Chen, T., et al. (2019). Genome-wide analysis identifies NR4A1 as a key mediator of T cell dysfunction. *Nature* 567, 525–529. <https://doi.org/10.1038/s41586-019-0979-8>.
44. Kortekaas Krohn, I., Aerts, J.L., Breckpot, K., Goyvaerts, C., Knol, E., Van Wijk, F., and Gutermuth, J. (2022). T-cell subsets in the skin and their role in inflammatory skin disorders. *Allergy* 77, 827–842. <https://doi.org/10.1111/all.15104>.
45. Martinez, F.O., Gordon, S., Locati, M., and Mantovani, A. (2006). Transcriptional profiling of the human monocyte-to-macrophage differentiation and polarization: new molecules and patterns of gene expression. *J. Immunol.* 177, 7303–7311. <https://doi.org/10.4049/jimmunol.177.10.7303>.
46. Willenborg, S., Injarabian, L., and Eming, S.A. (2022). Role of Macrophages in Wound Healing. *Cold Spring Harb. Perspect. Biol.* 14, a041216. <https://doi.org/10.1101/cshperspect.a041216>.
47. Willenborg, S., Sanin, D.E., Jais, A., Ding, X., Ulas, T., Nüchel, J., Popović, M., MacVicar, T., Langer, T., Schultze, J.L., et al. (2021). Mitochondrial metabolism coordinates stage-specific repair processes in macrophages during wound healing. *Cell Metab.* 33, 2398–2414.e9. <https://doi.org/10.1016/j.cmet.2021.10.004>.
48. Viola, A., Munari, F., Sánchez-Rodríguez, R., Scolaro, T., and Castegna, A. (2019). The Metabolic Signature of Macrophage Responses. *Front. Immunol.* 10, 1462. <https://doi.org/10.3389/fimmu.2019.01462>.
49. Nakamizo, S., Dutertre, C.A., Khalilnezhad, A., Zhang, X.M., Lim, S., Lum, J., Koh, G., Foong, C., Yong, P.J.A., Tan, K.J., et al. (2021). Single-cell analysis of human skin identifies CD14+ type 3 dendritic cells co-producing IL1B and IL23A in psoriasis. *J. Exp. Med.* 218, e20202345. <https://doi.org/10.1084/jem.20202345>.
50. Carlson, C.M., Endrizzi, B.T., Wu, J., Ding, X., Weinreich, M.A., Walsh, E.R., Wani, M.A., Lingrel, J.B., Hogquist, K.A., and Jameson, S.C. (2006). Kruppel-like factor 2 regulates thymocyte and T-cell migration. *Nature* 442, 299–302. <https://doi.org/10.1038/nature04882>.
51. Shao, T.-Y., Jiang, T.T., Stevens, J., Russi, A.E., Troutman, T.D., Bernieh, A., Pham, G., Erickson, J.J., Eshleman, E.M., Alenghat, T., et al. (2023).

- Kruppel-like factor 2+ CD4 T cells avert microbiota-induced intestinal inflammation. *Cell Rep.* 42, 113323. <https://doi.org/10.1016/j.celrep.2023.113323>.
52. Debes, G.F., and McGettigan, S.E. (2019). Skin-Associated B Cells in Health and Inflammation. *J. Immunol.* 202, 1659–1666. <https://doi.org/10.4049/jimmunol.1801211>.
 53. Browaeys, R., Gilis, J., Sang-Aram, C., Bleser, P.D., Hoste, L., Tavernier, S., Lambrechts, D., Seurinck, R., and Saeys, Y. (2023). MultiNicheNet: a flexible framework for differential cell-cell communication analysis from multi-sample multi-condition single-cell transcriptomics data. Preprint at bioRxiv. <https://doi.org/10.1101/2023.06.13.544751>.
 54. Siriwach, R., Ngo, A.Q., Higuchi, M., Arima, K., Sakamoto, S., Watanabe, A., Narumiya, S., and Thumke, D. (2022). Single-cell RNA sequencing identifies a migratory keratinocyte subpopulation expressing THBS1 in epidermal wound healing. *iScience* 25, 104130. <https://doi.org/10.1016/j.isci.2022.104130>.
 55. Liu, W., Hsu, D.K., Chen, H.Y., Yang, R.Y., Carraway, K.L., 3rd, Isseroff, R.R., and Liu, F.T. (2012). Galectin-3 regulates intracellular trafficking of EGFR through Alix and promotes keratinocyte migration. *J. Invest. Dermatol.* 132, 2828–2837. <https://doi.org/10.1038/jid.2012.211>.
 56. Banno, T., Gazel, A., and Blumenberg, M. (2004). Effects of Tumor Necrosis Factor- α (TNF α) in Epidermal Keratinocytes Revealed Using Global Transcriptional Profiling*. *J. Biol. Chem.* 279, 32633–32642. <https://doi.org/10.1074/jbc.M400642200>.
 57. Boro, M., and Balaji, K.N. (2017). CXCL1 and CXCL2 Regulate NLRP3 Inflammasome Activation via G-Protein-Coupled Receptor CXCR2. *J. Immunol.* 199, 1660–1671. <https://doi.org/10.4049/jimmunol.1700129>.
 58. Basbous, J., Chalbos, D., Hipskind, R., Jariel-Encontre, I., and Piechaczyk, M. (2007). Ubiquitin-independent proteasomal degradation of Fra-1 is antagonized by Erk1/2 pathway-mediated phosphorylation of a unique C-terminal destabilizer. *Mol. Cell. Biol.* 27, 3936–3950. <https://doi.org/10.1128/MCB.011776-06>.
 59. Jin, S., Guerrero-Juarez, C.F., Zhang, L., Chang, I., Ramos, R., Kuan, C.-H., Myung, P., Plikus, M.V., and Nie, Q. (2021). Inference and analysis of cell-cell communication using CellChat. *Nat. Commun.* 12, 1088. <https://doi.org/10.1038/s41467-021-21246-9>.
 60. Philippeos, C., Telerman, S.B., Oulès, B., Pisco, A.O., Shaw, T.J., Elgueta, R., Lombardi, G., Driskell, R.R., Soldin, M., Lynch, M.D., and Watt, F.M. (2018). Spatial and Single-Cell Transcriptional Profiling Identifies Functionally Distinct Human Dermal Fibroblast Subpopulations. *J. Invest. Dermatol.* 138, 811–825. <https://doi.org/10.1016/j.jid.2018.01.016>.
 61. Lange, M., Bergen, V., Klein, M., Setty, M., Reuter, B., Bakhti, M., Lickert, H., Ansari, M., Schniering, J., Schiller, H.B., et al. (2022). CellRank for directed single-cell fate mapping. *Nat. Methods* 19, 159–170. <https://doi.org/10.1038/s41592-021-01346-6>.
 62. Correa-Gallegos, D., Ye, H., Dasgupta, B., Sardogan, A., Kadri, S., Kandi, R., Dai, R., Lin, Y., Kopplin, R., Shenai, D.S., et al. (2023). CD201+ fascia progenitors choreograph injury repair. *Nature* 623, 792–802. <https://doi.org/10.1038/s41586-023-06725-x>.
 63. Seeger, M.A., and Paller, A.S. (2015). The Roles of Growth Factors in Keratinocyte Migration. *Adv. Wound Care (New Rochelle)* 4, 213–224. <https://doi.org/10.1089/wound.2014.0540>.
 64. Mata-Greenwood, E., Liao, W.X., Wang, W., Zheng, J., and Chen, D.B. (2010). Activation of AP-1 transcription factors differentiates FGF2 and vascular endothelial growth factor regulation of endothelial nitric-oxide synthase expression in placental artery endothelial cells. *J. Biol. Chem.* 285, 17348–17358. <https://doi.org/10.1074/jbc.M109.092791>.
 65. Liarte, S., Bernabé-García, Á., and Nicolás, F.J. (2020). Role of TGF- β in Skin Chronic Wounds: A Keratinocyte Perspective. *Cells* 9, 306. <https://doi.org/10.3390/cells9020306>.
 66. Bünemann, E., Hoff, N.-P., Bühren, B.A., Wiesner, U., Meller, S., Böлке, E., Müller-Homey, A., Kubitzka, R., Ruzicka, T., Zlotnik, A., et al. (2018). Chemokine ligand-receptor interactions critically regulate cutaneous wound healing. *Eur. J. Med. Res.* 23, 4. <https://doi.org/10.1186/s40001-017-0299-0>.
 67. Chang, T.-T., Chen, C., and Chen, J.-W. (2022). CCL7 as a novel inflammatory mediator in cardiovascular disease, diabetes mellitus, and kidney disease. *Cardiovasc. Diabetol.* 21, 185. <https://doi.org/10.1186/s12933-022-01626-1>.
 68. Pырillou, K., Burzynski, L.C., and Clarke, M.C.H. (2020). Alternative Pathways of IL-1 Activation, and Its Role in Health and Disease. *Front. Immunol.* 11, 613170. <https://doi.org/10.3389/fimmu.2020.613170>.
 69. Goumans, M.-J., Liu, Z., and ten Dijke, P. (2009). TGF- β signaling in vascular biology and dysfunction. *Cell Res.* 19, 116–127. <https://doi.org/10.1038/cr.2008.326>.
 70. Bossi, F., Tripodo, C., Rizzi, L., Bulla, R., Agostinis, C., Guarnotta, C., Munaut, C., Baldassarre, G., Papa, G., Zorzet, S., et al. (2014). C1q as a unique player in angiogenesis with therapeutic implication in wound healing. *Proc. Natl. Acad. Sci. USA* 111, 4209–4214. <https://doi.org/10.1073/pnas.1311968111>.
 71. Hayuningtyas, R.A., Han, M., Choi, S., Kwak, M.S., Park, I.H., Lee, J.-H., Choi, J.E., Kim, D.K., Son, M., and Shin, J.-S. (2021). The collagen structure of C1q induces wound healing by engaging discoidin domain receptor 2. *Mol. Med.* 27, 125. <https://doi.org/10.1186/s10020-021-00388-y>.
 72. Garoufalia, Z., Papadopetraki, A., Karatza, E., Vardakostas, D., Philippou, A., Kouraklis, G., and Mantas, D. (2021). Insulin-like growth factor-I and wound healing, a potential answer to non-healing wounds: A systematic review of the literature and future perspectives. *Biomed. Rep.* 15, 66. <https://doi.org/10.3892/br.2021.1442>.
 73. Wynn, T.A., and Vannella, K.M. (2016). Macrophages in Tissue Repair, Regeneration, and Fibrosis. *Immunity* 44, 450–462. <https://doi.org/10.1016/j.immuni.2016.02.015>.
 74. Usui, M.L., Mansbridge, J.N., Carter, W.G., Fujita, M., and Olerud, J.E. (2008). Keratinocyte migration, proliferation, and differentiation in chronic ulcers from patients with diabetes and normal wounds. *J. Histochem. Cytochem.* 56, 687–696. <https://doi.org/10.1369/jhc.2008.951194>.
 75. Stojadinovic, O., Pastar, I., Vukelic, S., Mahoney, M.G., Brennan, D., Krzyzanowska, A., Golinko, M., Brem, H., and Tomic-Canic, M. (2008). Deregulation of keratinocyte differentiation and activation: a hallmark of venous ulcers. *J. Cell. Mol. Med.* 12, 2675–2690. <https://doi.org/10.1111/j.1582-4934.2008.00321.x>.
 76. Ramirez, H.A., Pastar, I., Jozic, I., Stojadinovic, O., Stone, R.C., Ojeh, N., Gil, J., Davis, S.C., Kirsner, R.S., and Tomic-Canic, M. (2018). Staphylococcus aureus Triggers Induction of miR-15B-5P to Diminish DNA Repair and Deregulate Inflammatory Response in Diabetic Foot Ulcers. *J. Invest. Dermatol.* 138, 1187–1196. <https://doi.org/10.1016/j.jid.2017.11.038>.
 77. Eming, S.A., Krieg, T., and Davidson, J.M. (2007). Inflammation in Wound Repair: Molecular and Cellular Mechanisms. *J. Invest. Dermatol.* 127, 514–525. <https://doi.org/10.1038/sj.jid.5700701>.
 78. Martin, P., and Nunan, R. (2015). Cellular and molecular mechanisms of repair in acute and chronic wound healing. *Br. J. Dermatol.* 173, 370–378. <https://doi.org/10.1111/bjd.13954>.
 79. Krzyszczyk, P., Schloss, R., Palmer, A., and Berthiaume, F. (2018). The Role of Macrophages in Acute and Chronic Wound Healing and Interventions to Promote Pro-wound Healing Phenotypes. *Front. Physiol.* 9, 419. <https://doi.org/10.3389/fphys.2018.00419>.
 80. Guillamat-Prats, R. (2021). The Role of MSC in Wound Healing, Scarring and Regeneration. *Cells* 10, 1729. <https://doi.org/10.3390/cells10071729>.
 81. Tanaka, K., Ogino, R., Yamakawa, S., Suda, S., and Hayashida, K. (2022). Role and Function of Mesenchymal Stem Cells on Fibroblast in Cutaneous Wound Healing. *Biomedicines* 10, 1391. <https://doi.org/10.3390/biomedicines10061391>.
 82. Drinkwater, S.L., Burnand, K.G., Ding, R., and Smith, A. (2003). Increased but ineffectual angiogenic drive in nonhealing venous leg ulcers. *J. Vasc. Surg.* 38, 1106–1112. [https://doi.org/10.1016/S0741-5214\(03\)01053-X](https://doi.org/10.1016/S0741-5214(03)01053-X).
 83. Chamanga, E.T. (2018). Understanding venous leg ulcers. *Br. J. Community Nurs.* 23, S6–S15. <https://doi.org/10.12968/bjcn.2018.23.Sup9.S6>.

84. Haensel, D., Jin, S., Sun, P., Cinco, R., Dragan, M., Nguyen, Q., Cang, Z., Gong, Y., Vu, R., MacLean, A.L., et al. (2020). Defining Epidermal Basal Cell States during Skin Homeostasis and Wound Healing Using Single-Cell Transcriptomics. *Cell Rep.* 30, 3932–3947.e6. <https://doi.org/10.1016/j.celrep.2020.02.091>.
85. Foster, D.S., Januszky, M., Yost, K.E., Chinta, M.S., Gulati, G.S., Nguyen, A.T., Burcham, A.R., Salhotra, A., Ransom, R.C., Henn, D., et al. (2021). Integrated spatial multiomics reveals fibroblast fate during tissue repair. *Proc. Natl. Acad. Sci. USA* 118, e2110025118. <https://doi.org/10.1073/pnas.2110025118>.
86. Vu, R., Jin, S., Sun, P., Haensel, D., Nguyen, Q.H., Dragan, M., Kessenbrock, K., Nie, Q., and Dai, X. (2022). Wound healing in aged skin exhibits systems-level alterations in cellular composition and cell-cell communication. *Cell Rep.* 40, 111155. <https://doi.org/10.1016/j.celrep.2022.111155>.
87. Hu, K.H., Kuhn, N.F., Courau, T., Tsui, J., Samad, B., Ha, P., Kratz, J.R., Combes, A.J., and Krummel, M.F. (2023). Transcriptional space-time mapping identifies concerted immune and stromal cell patterns and gene programs in wound healing and cancer. *Cell Stem Cell* 30, 885–903.e10. <https://doi.org/10.1016/j.stem.2023.05.001>.
88. Shi, H., Cheer, K., Simanainen, U., Lesmana, B., Ma, D., Hew, J.J., Parungao, R.J., Li, Z., Cooper, M.S., Handelsman, D.J., et al. (2021). The contradictory role of androgens in cutaneous and major burn wound healing. *Burns Trauma* 9, tkaa046. <https://doi.org/10.1093/burnst/tkaa046>.
89. Cai, Y., Xiong, M., Xin, Z., Liu, C., Ren, J., Yang, X., Lei, J., Li, W., Liu, F., Chu, Q., et al. (2023). Decoding aging-dependent regenerative decline across tissues at single-cell resolution. *Cell Stem Cell* 30, 1674–1691.e8. <https://doi.org/10.1016/j.stem.2023.09.014>.
90. Liu, S., Hur, Y.H., Cai, X., Cong, Q., Yang, Y., Xu, C., Bilate, A.M., Gonzales, K.A.U., Parigi, S.M., Cowley, C.J., et al. (2023). A tissue injury sensing and repair pathway distinct from host pathogen defense. *Cell* 186, 2127–2143.e22. <https://doi.org/10.1016/j.cell.2023.03.031>.
91. Naldaiz-Gastesi, N., Goicoechea, M., Alonso-Martín, S., Aiastui, A., López-Mayorga, M., García-Belda, P., Lacalle, J., San José, C., Araúzo-Bravo, M.J., Trouilh, L., et al. (2016). Identification and Characterization of the Dermal Panniculus Carnosus Muscle Stem Cells. *Stem Cell Rep.* 7, 411–424. <https://doi.org/10.1016/j.stemcr.2016.08.002>.
92. Zomer, H.D., and Trentin, A.G. (2018). Skin wound healing in humans and mice: Challenges in translational research. *J. Dermatol. Sci.* 90, 3–12. <https://doi.org/10.1016/j.jdermsci.2017.12.009>.
93. Tauber, M., Basso, L., Martin, J., Bostan, L., Pinto, M.M., Thierry, G.R., Houmadi, R., Serhan, N., Loste, A., Blériot, C., et al. (2023). Landscape of mast cell populations across organs in mice and humans. *J. Exp. Med.* 220, e20230570. <https://doi.org/10.1084/jem.20230570>.
94. Pilcher, B.K., Dumin, J.A., Sudbeck, B.D., Krane, S.M., Welgus, H.G., and Parks, W.C. (1997). The activity of collagenase-1 is required for keratinocyte migration on a type I collagen matrix. *J. Cell Biol.* 137, 1445–1457. <https://doi.org/10.1083/jcb.137.6.1445>.
95. Hattori, N., Mochizuki, S., Kishi, K., Nakajima, T., Takaishi, H., D'Armiento, J., and Okada, Y. (2009). MMP-13 plays a role in keratinocyte migration, angiogenesis, and contraction in mouse skin wound healing. *Am. J. Pathol.* 175, 533–546. <https://doi.org/10.2353/ajpath.2009.081080>.
96. Eckert, R.L., Broome, A.-M., Ruse, M., Robinson, N., Ryan, D., and Lee, K. (2004). S100 Proteins in the Epidermis. *J. Invest. Dermatol.* 123, 23–33. <https://doi.org/10.1111/j.0022-202X.2004.22719.x>.
97. Sun, Y., Sheshadri, N., and Zong, W.X. (2017). SERPINB3 and B4: From biochemistry to biology. *Semin. Cell Dev. Biol.* 62, 170–177. <https://doi.org/10.1016/j.semcdb.2016.09.005>.
98. Madan, S., Uttekar, B., Chowdhary, S., and Rikhy, R. (2021). Mitochondria Lead the Way: Mitochondrial Dynamics and Function in Cellular Movements in Development and Disease. *Front. Cell Dev. Biol.* 9, 781933. <https://doi.org/10.3389/fcell.2021.781933>.
99. Gallini, S., Annusver, K., Rahman, N.-T., Gonzalez, D.G., Yun, S., Matte-Martone, C., Xin, T., Lathrop, E., Suozzi, K.C., Kasper, M., and Greco, V. (2023). Injury prevents Ras mutant cell expansion in mosaic skin. *Nature* 619, 167–175. <https://doi.org/10.1038/s41586-023-06198-y>.
100. Shao, Y., Chen, C., Shen, H., He, B.Z., Yu, D., Jiang, S., Zhao, S., Gao, Z., Zhu, Z., Chen, X., et al. (2019). GenTree, an integrated resource for analyzing the evolution and function of primate-specific coding genes. *Genome Res.* 29, 682–696. <https://doi.org/10.1101/gr.238733.118>.
101. Guo, C.J., Ma, X.K., Xing, Y.H., Zheng, C.C., Xu, Y.F., Shan, L., Zhang, J., Wang, S., Wang, Y., Carmichael, G.G., et al. (2020). Distinct Processing of lncRNAs Contributes to Non-conserved Functions in Stem Cells. *Cell* 181, 621–636.e22. <https://doi.org/10.1016/j.cell.2020.03.006>.
102. Jiang, Y., Tsoi, L.C., Billi, A.C., Ward, N.L., Harms, P.W., Zeng, C., Maverakis, E., Kahlenberg, J.M., and Gudjonsson, J.E. (2020). Cytokines: the diverse contribution of keratinocytes to immune responses in skin. *JCI Insight* 5, e142067. <https://doi.org/10.1172/jci.insight.142067>.
103. Landy, E., Carol, H., Ring, A., and Canna, S. (2024). Biological and clinical roles of IL-18 in inflammatory diseases. *Nat. Rev. Rheumatol.* 20, 33–47. <https://doi.org/10.1038/s41584-023-01053-w>.
104. Kroeze, K.L., Boink, M.A., Sampat-Sardjoepersad, S.C., Waaijman, T., Scheper, R.J., and Gibbs, S. (2012). Autocrine Regulation of Re-Epithelialization After Wounding by Chemokine Receptors CCR1, CCR10, CXCR1, CXCR2, and CXCR3. *J. Invest. Dermatol.* 132, 216–225. <https://doi.org/10.1038/jid.2011.245>.
105. Tsujihana, K., Tanegashima, K., Santo, Y., Yamada, H., Akazawa, S., Nakao, R., Tominaga, K., Saito, R., Nishito, Y., Hata, R.I., et al. (2022). Circadian protection against bacterial skin infection by epidermal CXCL14-mediated innate immunity. *Proc. Natl. Acad. Sci. USA* 119, e2116027119. <https://doi.org/10.1073/pnas.2116027119>.
106. Westrich, J.A., Vermeer, D.W., Colbert, P.L., Spanos, W.C., and Pyeon, D. (2020). The multifarious roles of the chemokine CXCL14 in cancer progression and immune responses. *Mol. Carcinog.* 59, 794–806. <https://doi.org/10.1002/mc.23188>.
107. Jiang, Z., Liu, Y., Li, C., Chang, L., Wang, W., Wang, Z., Gao, X., Ryyffel, B., Wu, Y., and Lai, Y. (2017). IL-36γ Induced by the TLR3-SLUG-VDR Axis Promotes Wound Healing via REG3A. *J. Invest. Dermatol.* 137, 2620–2629. <https://doi.org/10.1016/j.jid.2017.07.820>.
108. Saito, K., Iwata, Y., Fukushima, H., Watanabe, S., Tanaka, Y., Hasegawa, Y., Akiyama, M., and Sugiura, K. (2020). IL-36 receptor antagonist deficiency resulted in delayed wound healing due to excessive recruitment of immune cells. *Sci. Rep.* 10, 14772. <https://doi.org/10.1038/s41598-020-71256-8>.
109. Devalaraja, R.M., Nanney, L.B., Du, J., Qian, Q., Yu, Y., Devalaraja, M.N., and Richmond, A. (2000). Delayed Wound Healing in CXCR2 Knockout Mice. *J. Invest. Dermatol.* 115, 234–244. <https://doi.org/10.1046/j.1523-1747.2000.00034.x>.
110. Matar, D.Y., Ng, B., Darwish, O., Wu, M., Orgill, D.P., and Panayi, A.C. (2023). Skin Inflammation with a Focus on Wound Healing. *Adv. Wound Care (New Rochelle)* 12, 269–287. <https://doi.org/10.1089/wound.2021.0126>.
111. Monaghan, M.G., Borah, R., Thomsen, C., and Browne, S. (2023). Thou shall not heal: Overcoming the non-healing behaviour of diabetic foot ulcers by engineering the inflammatory microenvironment. *Adv. Drug Deliv. Rev.* 203, 115120. <https://doi.org/10.1016/j.addr.2023.115120>.
112. Phillipson, M., and Kubes, P. (2019). The Healing Power of Neutrophils. *Trends Immunol.* 40, 635–647. <https://doi.org/10.1016/j.it.2019.05.001>.
113. Vela-Romera, A., Carriel, V., Martín-Piedra, M.A., Aneiros-Fernández, J., Campos, F., Chato-Astrain, J., Prados-Olleta, N., Campos, A., Alaminos, M., and Garzón, I. (2019). Characterization of the human ridged and non-ridged skin: a comprehensive histological, histochemical and immunohistochemical analysis. *Histochem. Cell Biol.* 151, 57–73. <https://doi.org/10.1007/s00418-018-1701-x>.

114. Rinn, J.L., Bondre, C., Gladstone, H.B., Brown, P.O., and Chang, H.Y. (2006). Anatomic demarcation by positional variation in fibroblast gene expression programs. *PLoS Genet.* 2, e119. <https://doi.org/10.1371/journal.pgen.0020119>.
115. Rinn, J.L., Wang, J.K., Liu, H., Montgomery, K., van de Rijn, M., and Chang, H.Y. (2008). A systems biology approach to anatomic diversity of skin. *J. Invest. Dermatol.* 128, 776–782. <https://doi.org/10.1038/sj.jid.5700986>.
116. Cheng, J.B., Sedgewick, A.J., Finnegan, A.I., Harirchian, P., Lee, J., Kwon, S., Fassett, M.S., Golovato, J., Gray, M., Ghadially, R., et al. (2018). Transcriptional Programming of Normal and Inflamed Human Epidermis at Single-Cell Resolution. *Cell Rep.* 25, 871–883. <https://doi.org/10.1016/j.celrep.2018.09.006>.
117. Yan, Y., Tian, J., Wang, Y., Li, Y., Zhang, C., Zhang, S., Lin, P., Peng, R., Zhao, C., Zhuang, L., et al. (2023). Transcriptomic Heterogeneity of Skin Across Different Anatomic Sites. *J. Invest. Dermatol.* 143, 398–407.e5. <https://doi.org/10.1016/j.jid.2022.08.053>.
118. Butler, A., Hoffman, P., Smibert, P., Papalexi, E., and Satija, R. (2018). Integrating single-cell transcriptomic data across different conditions, technologies, and species. *Nat. Biotechnol.* 36, 411–420. <https://doi.org/10.1038/nbt.4096>.
119. Cao, J., Spielmann, M., Qiu, X., Huang, X., Ibrahim, D.M., Hill, A.J., Zhang, F., Mundlos, S., Christiansen, L., Steemers, F.J., et al. (2019). The single-cell transcriptional landscape of mammalian organogenesis. *Nature* 566, 496–502. <https://doi.org/10.1038/s41586-019-0969-x>.
120. Wu, T., Hu, E., Xu, S., Chen, M., Guo, P., Dai, Z., Feng, T., Zhou, L., Tang, W., Zhan, L., et al. (2021). clusterProfiler 4.0: A universal enrichment tool for interpreting omics data. *Innovation (Camb)* 2, 100141. <https://doi.org/10.1016/j.xinn.2021.100141>.
121. Aliee, H., and Theis, F.J. (2021). AutoGeneS: Automatic gene selection using multi-objective optimization for RNA-seq deconvolution. *Cell Syst.* 12, 706–715.e4. <https://doi.org/10.1016/j.cels.2021.05.006>.
122. Shannon, P., Markiel, A., Ozier, O., Baliga, N.S., Wang, J.T., Ramage, D., Amin, N., Schwikowski, B., and Ideker, T. (2003). Cytoscape: a software environment for integrated models of biomolecular interaction networks. *Genome Res.* 13, 2498–2504. <https://doi.org/10.1101/gr.1239303>.
123. Hafemeister, C., and Satija, R. (2019). Normalization and variance stabilization of single-cell RNA-seq data using regularized negative binomial regression. *Genome Biol.* 20, 296. <https://doi.org/10.1186/s13059-019-1874-1>.
124. Liu, T.-C., Kalugin, P.N., Wilding, J.L., and Bodmer, W.F. (2022). GMMchi: gene expression clustering using Gaussian mixture modeling. *BMC Bioinformatics* 23, 457. <https://doi.org/10.1186/s12859-022-05006-0>.
125. Love, M.I., Huber, W., and Anders, S. (2014). Moderated estimation of fold change and dispersion for RNA-seq data with DESeq2. *Genome Biol.* 15, 550. <https://doi.org/10.1186/s13059-014-0550-8>.
126. Ritchie, M.E., Phipson, B., Wu, D., Hu, Y., Law, C.W., Shi, W., and Smyth, G.K. (2015). limma powers differential expression analyses for RNA-sequencing and microarray studies. *Nucleic Acids Res.* 43, e47. <https://doi.org/10.1093/nar/gkv007>.
127. Ouyang, J.F., Kamaraj, U.S., Cao, E.Y., and Rackham, O.J.L. (2021). ShinyCell: simple and sharable visualization of single-cell gene expression data. *Bioinformatics* 37, 3374–3376. <https://doi.org/10.1093/bioinformatics/btab209>.
128. Li, T., Horsfall, D., Basurto-Lozada, D., Roberts, K., Prete, M., Lawrence, J.E.G., He, P., Tuck, E., Moore, J., Yoldas, A.K., et al. (2024). WebAtlas pipeline for integrated single-cell and spatial transcriptomic data. *Nat. Methods.* <https://doi.org/10.1038/s41592-024-02371-x>.

STAR★METHODS

KEY RESOURCES TABLE

REAGENT or RESOURCE	SOURCE	IDENTIFIER
Antibodies		
FOSL1	CellSignaling Technology	Cat#5281;RRID:AB_10557418
p-FOSL1	CellSignaling Technology	Cat#3880; RRID:AB_2106922
ERK	CellSignaling Technology	Cat#4695; RRID:AB_390779
p-ERK	CellSignaling Technology	Cat#4370; RRID:AB_2315112
GAPDH	HUABIO	Cat#ET1601-4; RRID:AB_3069615
Fra1 Polyclonal Antibody	Thermofisher	Cat#PA5-40361; RRID:AB_2609389
Alexa Fluor® 488 Mouse monoclonal [KP1] to CD68	Abcam	Cat#ab222914
Anti-IL-1 beta antibody [OTI3E1]	Abcam	Cat#ab156791; RRID:AB_2890254
EREG	Thermofisher	Cat#PA5-46969; RRID:AB_2610406
MKI67	CellSignaling Technology	Cat#9449; RRID:AB_2797703
S100A7	Abcam	Cat#ab13680; RRID:AB_300557
EREG (Mouse)	R&D	Cat#AF1068; RRID:AB_2293459
F4/80 (Mouse)	Santa Cruz	Cat#sc-52664; RRID:AB_629466
MKI67 (Mouse)	Thermo Fisher	Cat#MA5-14520; RRID:AB_10979488
FOSL1 (Mouse)	Novus Bio	Cat#NBP1-47757; RRID:AB_10010724
S100A7 (Mouse)	Boster Biological Technology	Cat#A02369
Biological samples		
Human wound samples	Karolinska Institutet Biobank	N/A
Human plastic surgery samples	Karolinska Institutet Biobank	N/A
Human venous ulcer samples	Dermatology Hospital of Chinese Academy of Medical Sciences	N/A
Mouse wound samples (WT and DB)	Cyagen Biosciences	N/A
Chemicals, peptides, and recombinant proteins		
Dynabeads™ MyOne™ Streptavidin C1	Thermo Fisher	65001
Pierce™ Protein A/G Magnetic Beads	Thermo Fisher	88802
Pierce™ 16% Formaldehyde (w/v), Methanol-free	Thermo Fisher	28906
Glycine	Sigma-Aldrich	50046
ProLong™ Diamond Antifade Mountant with DAPI	Thermo Fisher	P36966
TRIzol™ Reagent	Thermo Fisher	15596018
Red Blood Cell Lysis Solution	Miltenyi Biotec	130-094-183
EpiLife™ Medium, with 60 μM calcium	Thermo Fisher	MEPI500CA
Human Keratinocyte Growth Supplement (HKGS)	Thermo Fisher	S0015
DMEM, high glucose	Thermo Fisher	11965092
TritonX100	Merck	X100-100ML
Dispase II, powder	Thermo Fisher	17105041
Recombinant Human TNF-alpha Protein	R&D Systems	210-TA-020
BSA	Merck	10711454001
Pierce™ IP Lysis Buffer	Thermo Fisher	87787
Recombinant Proteinase K Solution (20 mg/mL)	Thermo Fisher	AM2546
2x Laemmli Sample Buffer	Bio-Rad Laboratories	1610737EDU
AREG (20ng/mL)	Novoprotein	CG04
TGFalpha (20ng/mL)	SinoBiological	11252-HNAE
HB-EGF (20ng/mL)	SinoBiological	10325-HNAB
HGF (20ng/mL)	Novoprotein	CJ72

(Continued on next page)

Continued

REAGENT or RESOURCE	SOURCE	IDENTIFIER
ANGPTL4 (500ng/mL)	Novoprotein	CW53
EREG (20ng/mL)	GenScript	Z02865
APRIL (TNFSF13) (500ng/mL)	Novoprotein	Cat. No.:CU89
CXCL6 (20ng/mL)	Novoprotein	C598
ADAM17 (50ng/mL)	Proteintech	Ag32418
LTB (20ng/mL)	Abmart	RKRB5609S
CXCL1 (20ng/mL)	Novoprotein	C597
CXCL5 (20ng/mL)	Novoprotein	CF14
IL1B (20ng/mL)	Novoprotein	CG93

Critical commercial assays

Whole Skin Dissociation Kit, human	Miltenyi Biotec	130-101-540
Dead Cell Removal Kit	Miltenyi Biotec	130-090-101
Pierce™ RNA 3' End Desthiobiotinylation Kit	Thermo Fisher	20163
Chromium Next GEM Single Cell 3' Reagent Kits v3.1, 16 rxns	10X Genomics	PN-1000268
Chromium Next GEM Chip G Single Cell Kit, 48 rxns	10X Genomics	PN-1000120
Dual Index Kit TT Set A	10X Genomics	PN-1000215
RNAscope® Multiplex Fluorescent Reagent Kit v2	Advanced Cell Diagnostics, Inc	323100
Visium Spatial Gene Expression Slide & Reagents Kit	10X Genomics	1000187
Visium Spatial Gene Expression Starter Kit	10X Genomics	1000200
Visium Spatial Tissue Optimization Slide & Reagents Kit	10X Genomics	1000193
RevertAid First Strand cDNA Synthesis Kit	Thermo Fisher	K1622
Power SYBR™ Green PCR Master Mix	Thermo Fisher	4368708
TaqMan™ Universal PCR Master Mix	Thermo Fisher	4304437

Deposited data

Human skin acute wound single-cell RNA-seq data	This paper	GEO: GSE241132
Human venous ulcer single-cell RNA-seq data	This paper	GEO: GSE265972
Human skin acute wound spatial transcriptomics data	This paper	GEO: GSE241124
Mouse wound data (UW+PWD3)	This paper	GEO: GSE218430
Mouse wound data (UW+PWD2+PWD4+PWD7)	Cai et al. ⁸⁹	GSA: CRA010641
Single-cell RNA-seq datasets from human healthy adult skin and inflamed skin diseases	Reynolds et al. ²⁰	E-MATB-8142
Diabetic foot ulcers single-cell RNA-seq data	Theocharidis et al. ⁷	GEO: GSE165816
Human acute wound skin bulk RNA-seq data	Liu et al. ¹²	GEO: GSE174661

Experimental models: Cell lines

Human Epidermal Keratinocytes, adult (HEKa)	Thermo Fisher	C0055C
---	---------------	--------

Oligonucleotides

FISH probe: MMP3	ACD company	#403421
FISH probe: KRT6B	ACD company	#805641
FISH probe: ADAM12	ACD company	#432561
qPCR primer: FOSL1	Sangon	Forward: TGACCACACCCTCCCTAACTC
qPCR primer: FOSL1	Sangon	Reverse: CTGCTGCTACTCTTGCGATGA
qPCR primer: CXCL1	IDT	Hs.PT.58.39039397
qPCR primer: GAPDH	IDT	Hs.PT.39a.22214836
siRNA: siFOSL1	GenePharma	Sense: GAGGGCAGCUGCUAUUUAUTT
siRNA: siFOSL1	GenePharma	Antisense: AUAAAUAGCAGCUGCCCUCTT

Software and algorithms

CellRanger v5.0.1	10X genomics	https://www.10xgenomics.com/support/single-cell-gene-expression
-------------------	--------------	---

(Continued on next page)

Continued

REAGENT or RESOURCE	SOURCE	IDENTIFIER
Spaceranger v1.2.0	10X genomics	https://www.10xgenomics.com/support/software/space-ranger
R v4.1.1 and v4.2.3	R Core Team	https://www.r-project.org/
RStudio	Posit	https://posit.co/download/rstudio-desktop/
Seurat v4	Hao et al. ¹⁸	https://github.com/satijalab/seurat/
Scrublet v0.2.3	Wolock et al. ¹⁶	https://github.com/swolock/scrublet
DoubletFinder v2.0.3	McGinnis et al. ¹⁷	https://github.com/chris-mcginnis-ucsf/DoubletFinder
Harmony v0.1	Korsunsky et al. ²⁸	https://github.com/immunogenomics/harmony
Canonical correlation analysis (CCA)	Butler et al. ¹¹⁸	https://github.com/satijalab/seurat/
MiloR v1.6.0	Dann et al. ²⁹	https://github.com/MarioniLab/miloR
pySCENIC v0.11.2	Aibar et al. ³⁵	https://scenic.aertslab.org/
CellOracle v0.10.14	Kamimoto et al. ³⁹	https://github.com/morris-lab/CellOracle
scikit-learn python package (Gaussian Mixture Model)	https://scikit-learn.org/stable/	https://scikit-learn.org/stable/
Monocle3	Cao et al. ¹¹⁹	https://cole-trapnell-lab.github.io/monocle3
CellRank v1	Lange et al. ⁶¹	https://cellrank.org
clusterProfiler v4	Wu et al. ¹²⁰	https://github.com/YuLab-SMU/clusterProfiler
MultiNicheNet	Browaeys et al. ⁵³	https://github.com/saeyslab/multinichenetr
CellChat (v1.4.0)	Jin et al. ⁵⁹	https://github.com/sqjin/CellChat
Cell2location	Kleshchevnikov et al. ²⁷	https://github.com/BayraktarLab/cell2location/
AutoGeneS	Aliee and Theis ¹²¹	https://github.com/theislab/AutoGeneS
Cytoscape v3.8.2	Shannon et al. ¹²²	https://cytoscape.org/
Image J	NIH	https://imagej.nih.gov/ij
BioRender	https://www.biorender.com	https://www.biorender.com
Custom code	This study	https://doi.org/10.5281/zenodo.14176654

EXPERIMENTAL MODEL AND STUDY PARTICIPANT DETAILS

Human wound sample collection

Five healthy volunteers were enrolled at the Karolinska University Hospital, Stockholm, Sweden. Three full-thickness skin wounds were created on the upper buttock area of each donor using a 4-mm biopsy punch. Wound edge tissues were collected on days 1, 7, and 30 using a 6-mm biopsy punch. The samples were transferred to the laboratory for single-cell RNA sequencing (10X Genomics) or snap-frozen for spatial transcriptomics (10X Genomics). Written informed consent was obtained from all donors for the collection and use of tissues for research. This study was approved by the Stockholm Regional Ethics Committee and conducted according to the Declaration of Helsinki's principles.

Venous ulcer samples and age- and body-location-matched healthy control samples from nine donors were collected at the Dermatology Hospital of Chinese Academy of Medical Sciences, Nanjing, China. Patients with apparent soft tissue infections or requiring systemic antibiotic treatment were excluded. After obtaining written informed consent from the patients, chronic wound edge tissue samples were collected using a 4-mm biopsy punch following a local lidocaine injection. This study was approved by the Ethics Committee of Institute of Dermatology, Chinese Academy of Medical Sciences (Ethic permission number: 2021-KY-059).

Mice wound sample collection

C57BL/6J wild-type mice were obtained from Charles River Laboratories (Sulzfeld, Germany) and housed under pathogen-free conditions at the Comparative Medicine Biomedicum (KMB) facility, Karolinska Institutet. They were maintained under standard conditions with free access to food and water, a 12-hour light/dark cycle, controlled temperature (20–22°C), and humidity (40–60%). Mice aged 8–10 weeks were used for the experiments, approved by the Swedish Board of Agriculture's Committee on Animal Experimentation (Jordbruksverket).

Prior to wounding, 8-week-old mice with back skin in the telogen (resting) phase of the hair cycle were shaved and treated with depilatory cream. A 4-mm full-thickness wound, extending through the panniculus carnosus, was created on the back using a biopsy punch. Post-surgery, mice were housed individually to prevent interference. Buprenorphine (0.03 mg/kg, subcutaneous) was administered twice daily for the first two days to manage pain. On day 3 post-wounding, wound-edge and intact skin samples (at least 1.5 cm from the wound) were collected using a 6-mm biopsy punch for single-cell sequencing.

METHOD DETAILS

Human and mouse single-cell RNA sequencing

We followed the same protocol to prepare single-cell suspensions from human and mouse skin and wound samples. Briefly, tissues were incubated in 5 U/ml Dispase II at 4°C overnight. The epidermis was then gently separated from the dermis and incubated in 0.025% Trypsin/EDTA (Thermo Fisher) for 10–15 minutes at 37°C. The dermal cell suspension was prepared using the Whole Skin Dissociation Kit (Miltenyi Biotec) per the manufacturer's instructions. To capture a broad range of cell types, equal amounts of epidermal and dermal cells were mixed. Red blood cells and dead cells were removed using the Red Blood Cell Removal Solution and Dead Cell Removal Kit (both from Miltenyi Biotec). After purification, viable cells were loaded onto the Chromium Controller (10X Genomics) for single-cell encapsulation and cDNA library generation using the Chromium Next GEM Single Cell 3' Reagent Kits v3.1 (10X Genomics). Libraries were sequenced on an Illumina NovaSeq6000 platform, with an average of 50K read-pairs per cell.

Spatial transcriptomic sequencing

Fresh frozen skin and acute wound tissues were embedded in the Optimal Cutting Temperature compound (OCT, Sakura Tissue-TEK) on dry ice. Sections were fixed in methanol and imaged after hematoxylin and eosin (H&E) staining to assess the morphology and quality of the tissues. The optimal permeabilization time for wound sections was determined to be 15 minutes following the manufacturer's instructions (10X Genomics, Visium Spatial Tissue Optimization). Spatial gene expression libraries from 16 wound skin sections were then generated according to the instructions of the Visium Spatial Gene Expression Kit from 10X Genomics. The libraries were sequenced using the Illumina NovaSeq6000 platform to generate approximately 150 M read-pairs per section.

Human scRNA-seq data processing

The single-cell sequence data were mapped with Cell Ranger (version 5.0.1) to a manually built human reference genome GRCh38 with the annotation file GENCODE version 38. The raw gene expression matrix contained 65,462 cells and 27,973 genes. The low-quality cells expressing <500 genes, >20% mitochondrial genes, and <1000 gene counts were filtered out. Mitochondrial and hemoglobin genes, as well as genes expressed in fewer than ten cells, were excluded. Potential doublets were detected using Scrublet¹⁶ (v0.2.3) and DoubletFinder¹⁷ (v2.0.3). Cells identified as doublets by both tools or those in clusters with multiple distinct cell type markers were excluded. In total, 58,823 cells and 25,778 genes from 12 samples of acute wounds were retained for downstream analysis.

Data normalization and scaling were performed using the SCTransform¹²³ package, regressing out mitochondrial percentage and cell cycle effects. Cell cycle analysis was conducted using the CellCycleScoring function based on the normalized gene expression. The top 4000 variable genes were used for principal component analysis (PCA). During data integration, sample-to-sample batch effects were corrected using top 40 PCs as input for the RunHarmony²⁸ function. Uniform Manifold Approximation and Projection (UMAP) and k-nearest neighbors graph were generated using the RunUMAP and FindNeighbors functions in Seurat¹⁸ (v4), respectively. Major cell clusters were identified using the Louvain graph-based algorithm with a resolution of 0.8, resulting in 27 clusters. Differentially expressed genes among clusters were calculated using the FindAllMarkers functions with the MAST method. Genes with adjusted Pvalue<0.05, log fold change>0.25, and detected in at least 25 percent of cells were considered significantly high in the cluster. Clusters were annotated based on each cluster's top marker genes ranked by fold changes and well-documented signature genes of distinct cell types.

Before sub-clustering analysis, cells of low-quality keratinocyte cluster Bas-II from major clusters were filtered out. Subpopulation analyses of keratinocytes, fibroblasts, angiogenic cells, myeloid cells, and lymphoid cells were performed individually using the same pipeline as for major cluster identification, including normalization, variable feature selection, batch correction, dimensionality reduction, and unsupervised clustering, but with a resolution of 0.5.

Neutrophil analysis was performed using unfiltered count matrices of samples after running Cell Ranger. Cells with fewer than 100 expressed genes were filtered out, retaining only those not included in the above analysis. Initial neutrophils were selected based on the expression profiles of well-known markers (FCGR3B, CMTM2, CXCR2, PROK2, LINC01506).⁴² Cells were further filtered after clustering analysis based on the neutrophil scores of each cluster. The refined neutrophils were extracted and re-ran the normalization, scaling, and clustering steps with a resolution of 0.3.

Mouse single-cell sequencing data processing

The mouse single-cell data were processed using a protocol similar to the one used for human data. Raw sequencing data were analyzed with the 10X Cell Ranger (v5.0.1) pipeline, which included demultiplexing, alignment to the GRCm39 (mm39) mouse genome, barcode counting, and unique molecular identifier (UMI) quantification. Predicted doublets were removed based on Scrublet analysis. The filtered feature-barcode matrices were further processed using the Seurat pipeline. Cells expressing fewer than 500 genes, fewer than 1000 UMIs, or more than 10% mitochondrial genes, as well as mitochondrial, hemoglobin, ribosomal genes, and genes expressed in fewer than 10 cells, were excluded. Data normalization was performed using SCTransform. Principal component analysis (PCA) was applied to the top 4000 variable genes, and the first 40 principal components (PCs), as determined by ElbowPlot, were used in the RunHarmony function to correct for batch effects across libraries. Uniform manifold approximation and projection

(UMAP) plots were generated using RunUMAP with the first 40 harmonized PCs. Clustering was performed using FindNeighbors and FindClusters with a resolution of 0.8, and cluster markers were identified with FindAllMarkers. Cell types were annotated based on known signature genes from previous studies.

Differential abundance testing with Milo

We tested for differential cell-state abundances of subpopulations across wound healing using the MiloR package (v1.6.0).²⁹ Specifically, a K-nearest neighbors (KNN) graph was built using the graph 'HARMONY' slot from the adjacency matrix of the processed Seurat object with the parameters: $k = 40$ and $d=30$. Cells were assigned to the neighborhoods based on the KNN graph using the 'makeNhoods' function ($\text{prop}=0.1$). To explore variations in cell counts between neighboring wound healing points (pairwise comparisons), cells from each sample in each neighborhood were counted. Differential neighborhood abundance testing was performed using a generalized linear model (GLM). Differentially abundant cell neighborhoods with $\text{SpatialFDR} \leq 0.1$ were plotted using the 'plotNhoodGraphDA' function.

SCENIC and CellOracle analyses

The pySCENIC (v0.11.2)³⁵ was utilized to investigate the role of transcriptional regulators in human skin wound healing, following the package's tutorial. Raw count expression matrices of cell types were first prepared to construct co-expression modules between transcription factors (TFs hg38) and potential target genes ranked by importance. Modules showing significant motif enrichment remained, and TFs with directed targets in these modules were defined as regulons. Each regulon was then assigned an activity score using the AUcell function. The top 5 regulons for each cell type were highlighted based on the scaled activity Z-scores across other cell types. The regulon network was visualized using Cytoscape¹²² (v3.8.2) software.

In silico TF perturbation of gene regulatory networks (GRNs) was performed using CellOracle (v0.10.14)³⁹ package. Based on a pre-built GRN of human (hg38) from curated transposase-accessible chromatin with sequencing (ATAC-seq) data, we simulated cell identity shifts in response to TF FOSL1 knockout and overexpression, setting the expression value to 0 and 2, respectively. The simulated overexpression value exceeded the detected gene expression. Subsequently, we compared the simulated TF perturbation vector field with the natural development vector field by calculating the perturbation score (PS). Positive and negative PSs denoted the promotion and inhibition of cell differentiation, respectively.

Trajectory analysis of keratinocytes and fibroblasts

To infer the differences in epidermal cell trajectories between intact skin and wound conditions, we separated all keratinocytes into wound and non-wound cells using a Gaussian mixture model (GMM) in the 'scikit-learn' Python package.¹²⁴ We first filtered out cells that did not express KRT6A, a strong marker of wound-induced cells.^{30,31} The positive cells were categorized into '0' and '1' classes, representing low- ($KRT6A^{dim}$) and high-expressing ($KRT6A^+$) cells. The wound cells comprised $KRT6A^+$ cells, while the rest of the keratinocytes ($KRT6A^{dim}/KRT6A^-$) were defined as non-wound cells. Pseudotime trajectory analysis of wound and non-wound keratinocytes was performed using Monocle3¹¹⁹ package. The basal cell cluster (Bas-I) was selected as a starting point of the pseudotime trajectory. The differentially expressed driving genes along the trajectory were determined using Moran's I test in the 'graph_t-est' function, with the filtering criteria: $q_value < 0.00001$ and $morans_I > 0.25$.

RNA velocity analysis of fibroblasts was carried out using the CellRank (version 1)⁶¹ package, which predicted the cell differentiation trajectory and its directionality based on the spliced and unspliced mRNA content. The initial and terminal states were identified using a deterministic mode in 'cr.tl.initial_states' and 'cr.tl.terminal_states' functions.

Gene ontology analysis

Gene ontology (GO) analysis of all gene clusters was computed using the Fisher exact test in the clusterProfiler¹²⁰ package. GO biological process (BP) terms were filtered by the adjusted P value < 0.05 and enriched gene count > 5 .

M1 and M2 signature

Pro-inflammatory macrophage (M1) and anti-inflammatory macrophage (M2) signatures were derived from Table 1 published by Martinez et al.⁴⁵ Those in common with top marker genes of macrophage clusters were used to calculate the M1- and M2-like scores using the 'AddModuleScore' function in the Seurat package.¹⁸

Cell-to-cell communication analysis

To study putative cell-cell interactions across the wound healing process, we used the MultiNicheNet⁵³ R package to infer the ligand-receptor pairs in the acute wound scRNA-seq dataset. The MultiNicheNet is a framework based on prior knowledge of ligand-receptor and ligand-target networks (version 2) that better explores cell-cell communications from multi-sample, multi-condition scRNA-seq data. Significant ligand-receptor pairs between cell types were determined by the high expression of each pair, as well as differentially expressed target genes of ligands in receiving cell types of different conditions, using the 'multi_nichenet_analysis' function with criteria: $\text{min_cells}=10$, $\text{logFC_threshold}=0.50$, $\text{p_val_threshold}=0.05$, $\text{fraction_cutoff}=0.05$, $\text{top_n_target}=250$.

In addition, we applied the CellChat⁵⁹ package to perform differential signaling changes within basal and spinous migrating keratinocytes between intact skin and wound conditions. Cells from each condition were imported into the CellChat analysis individually. The major signaling contributors of each cell type were calculated based on signaling network likelihoods using the

'netAnalysis_computeCentrality' function with a threshold of $p\text{-value} < 0.05$. The differential outgoing and incoming interaction strengths of each cell population in the cell-cell communication network between the two conditions were computed using the 'netAnalysis_signalingRole_scatter' function.

ST-seq data processing

Spatial sequencing data of human acute wounds was mapped to the GRCh38 human genome using Space Ranger (v1.2). Spots with less than 100 genes expressed and in low-quality clusters were excluded. We also filtered out *MALAT1*, mitochondrial, and hemoglobin-related genes. In total, 22,915 spots and 36,578 genes from 16 sections remained. The data normalization and batch correction were performed using SCTransform¹²³ and Harmony,²⁸ respectively. Dimensionality reduction, clustering (res=0.5), UMAP, and differentially expressed genes (DEGs) were carried out using the Seurat (v4)¹⁸ package. Spot clusters were annotated based on DEGs and markers of distinct cell types from scRNA-seq. Spatial cell type distribution and gene expression were visualized using the 'SpatialDimPlot' and 'SpatialFeaturePlot' functions, respectively.

Pseudobulk analysis of scRNA-seq and ST-seq

To examine the sample or donor heterogeneity in scRNA-seq and ST-seq, we performed the similarity analysis using the gene counts generated from converting the gene expression of single-cell and spatial data to pseudobulk sequencing data. The principal component and distance among samples were calculated using the R DESeq2 package.¹²⁵ Pseudobulk differential expression analysis was carried out using DESeq2¹²⁵ and limma¹²⁶ R packages. Significantly expressed genes were defined with $\text{avg_log2FC} > 1$ and $p\text{-value_adj} < 0.05$. The top 500 (ranked by fold changes) significant DE genes were used for GO analysis.

Deconvolution of ST-seq data and wound bulk RNA-seq data

To spatially map wound cell states defined by scRNA-seq data profiles in the Visium data, we used the Cell2location²⁷ package. In brief, we trained a negative binomial regression model to estimate reference transcriptomic signatures based on each cell type's top 100 marker genes profiled by scRNA-seq. We estimated the abundance of every cell type in each Visium spot using the inferred reference cell type signatures by decomposing spot mRNA counts. All parameters were set to default except for two: 1) the expected cell abundance ($N\text{-cells_per_location} = 20$) determined by approximately counting the average numbers of nuclei of each spot in H&E images, and 2) regularisation of per-location normalization ($\text{detection_alpha} = 20$) to account for large variations in RNA detection sensitivity across different spots on Visium slides. The posterior distribution of cell abundance for each cell type in each spot was summarized as 5% quantile, representing high confidence, which was used for visualization and colocalization analysis. To identify microenvironments of spatial co-occurrence of cell types, we performed a non-negative matrix factorization (NMF) analysis of the high-confidence cell type abundances, setting the number of factors to $R = 15$. A cell type was considered localized in a microenvironment if its fraction was over 0.1.

Bulk RNA sequencing data of intact skin and wounds (Day 1 and Day 7 post-wounding) from our previous study¹² (GSE174661) was deconvoluted using the AutoGeneS¹²¹ package. Centroids of cell types were first constructed from our scRNA-seq data of acute wounds using the top 4000 highly variable genes and distinct markers of each cell type. The bulk data was then deconvoluted based on these centroids using a regression method of Nu-support vector machine (Nu-SVR).

Venous ulcer scRNA-seq analysis

scRNA-seq data from cells with < 500 genes expressed, $> 20\%$ mitochondrial genes, or < 1000 gene counts were excluded. After quality control, a total of 48,346 cells from four venous ulcers (VU) and five matched healthy controls were analyzed using the same workflow and criteria as for acute wound scRNA-seq.

Integration of wounded skin scRNA-seq datasets

We retrieved public scRNA-seq datasets of healthy adult skin from Reynolds et al.²⁰ (2021, E-MTAB-8142) and diabetic foot ulcers (DFU) from Theocharidis et al.⁷ (2022, GSE165816). For the DFU scRNA-seq, we included 9 healthy controls and two subgroups of DFU patients: those who healed the ulcers (Healer, DFU_H $n = 7$) and those who failed to heal within 12 weeks post-surgery (Non-healer, DFU_NH $n = 4$). Data integration across different scRNA-seq datasets, including acute wounds, VU, DFU, and human adult skin, was carried out using the Harmony²⁸ algorithm, setting each sample as a group variable.

Cell label transfer was performed using the 'FindTransferAnchors' and 'MapQuery' functions in Seurat,¹⁸ setting the cell types generated from our acute wound dataset as a reference. The average predicted scores of each cell type were used to assess the correlation of cell types across different scRNA-seq datasets. Furthermore, we refined cell labels using integrated unsupervised clustering results, resolving ambiguous assignments by aligning them with the majority cell type in each population to enable a precise comparison of cellular heterogeneity between acute and chronic wounds.

Cross-species comparison of human and mouse wound healing

To compare human and mouse wound healing, we integrated scRNA-seq data of human and mouse acute wounds at the inflammatory phase (GSE218430) using canonical correlation analysis (CCA). Before integration, we sampled the same number of cells from each sample in both datasets. The overlapped homologous genes of humans and mice were kept for integration. CCA¹¹⁸ in Seurat (v4)¹⁸ was used to integrate the human and mouse scRNA-seq datasets using the top 3000 variable genes and each sample as an

integration anchor. The dynamic changes of cellular proportions of human-mouse joint clusters were traced according to the original cell-type assignments using the Sankey diagram. Conserved markers of integrated clusters were identified using the Seurat 'FindConservedMarkers' function. Differential expression analysis between human and mouse migrating keratinocytes was performed using the MAST test in Seurat 'FindMarkers' function.¹⁸ Functional enrichment of DEGs in humans and mice was carried out using clusterProfiler,¹²⁰ and the top 6 significant BP terms (adjusted Pvalue<0.05 and enriched gene count>5) were plotted. Cross-species comparison of migration and proliferation scores in integrated migrating and proliferating clusters was calculated based on the top 10 conserved marker genes across species using the Seurat 'AddModuleScore' function.

To further investigate the dynamic spatiotemporal changes across human and mouse wound healing, we used another publicly available mouse wound data⁸⁹ (accession number: GSA: CRA010641) that contained the unwounded skin (UW), post-wounding day 2, 4, and 7 (PWD2, PWD4, PWD7). After sampling the cell numbers for each condition across species, the integrated data were analyzed using the same pipeline as above described.

Human-specific coding and non-coding genes were retrieved from previous literature,^{100,101} and their expression was visualized using the Seurat 'DoHeatmap' function.

Fluorescent *in situ* hybridization (FISH)

Probes for MMP3, KRT6B, and ADAM12 (Hs-MMP3:#403421, Hs-KRT6B:#805641, Hs-ADAM12:#432561) were designed by Advanced Cell Diagnostics (ACD) in Silicon Valley, CA. Human skin and wound slides were prepared according to the manufacturer's instructions. After fixation and dehydration using 50%, 70%, and 100% ethanol, the slides were treated with Protease IV (ACD) and incubated at room temperature for 30 minutes. Subsequently, the slides were incubated with the probes for two hours at 40 °C, using the HybEZ™ II Hybridization System and the RNAscope® Multiplex Fluorescent Reagent Kit v2 (ACD). The hybridization signals were amplified per the manufacturer's instructions and captured using a Zeiss Axio Scan Z1 slide scanner.

Immunofluorescence staining and microscopy

Paraffin-embedded tissue sections were deparaffinized and rehydrated using xylene and a series of graded ethanol solutions. Antigen retrieval was performed in citric acid buffer (10 mM, pH 6.0). The sections were then blocked with 2.5% bovine serum albumin (BSA) in Tris-buffered saline with 0.1% Tween-20 (TBST). Next, the sections were incubated overnight at 4°C with primary antibodies specific to the anti-human FOSL1 (1:100 dilution, ThermoFisher, #PA5-40361), anti-human IL1b (1:150 dilution, Abcam, ab156791), anti-human CD68 (1:100 dilution, conjugated with Alexa Fluor® 488, Abcam, ab222914), anti-human EREG (1:200 dilution, ThermoFisher, PA5-46969), anti-human MKI67 (1:400 dilution, CST, 9449) and anti-human S100A7 (1:200, Abcam, ab13680), anti-mouse EREG (1:100 dilution, R&D, AF1068), anti-mouse F4/80 (1:150 dilution, Santa Cruz, Sc-52664), anti-mouse MKI67 (1:150 dilution, Thermo Fisher, MA5-14520), anti-mouse FOSL1 (1:110 dilution, Novus Biologicals, NBP1-47757) and anti-mouse S100A7 (1:200, Boster Biological Technology, A02369). After primary antibody incubation, the sections were treated with Alexa Fluor 555 Donkey anti-Rabbit IgG (H+L) Highly Cross-Adsorbed secondary antibody (cat. A-31572, ThermoFisher Scientific) or Goat anti-Mouse IgG (H+L) Highly Cross-Adsorbed Secondary Antibody, Alexa Fluor Plus 647 (cat. A-32728, ThermoFisher Scientific) or Alexa Fluor™ 488 Donkey anti-Rat IgG (H+L) Highly Cross-Adsorbed secondary antibody (A-21208, ThermoFisher Scientific) or Alexa Fluor™ 555 Donkey anti-Goat IgG (H+L) Cross-Adsorbed Secondary Antibody (A-21432, ThermoFisher Scientific) diluted at 1:1000 in TBST. To visualize cell nuclei, we counter-stained the sections with DAPI and mounted them using an anti-fading polyvinyl alcohol mounting medium (ThermoFisher Scientific). Immunofluorescence staining was observed using a Confocal fluorescence microscope.

RNA extraction and qRT-PCR

Total RNA was isolated from human *in vivo* wounds using the miRNeasy mini kit (Qiagen), followed by cDNA synthesis using the RevertAid First Strand cDNA Synthesis Kit (ThermoFisher Scientific). Specific premixed primers and probes for CXCL1 and GAPDH were designed by Integrated DNA Technologies (IDT, Leuven, Belgium). Gene expression levels were quantified using TaqMan expression assays (ThermoFisher Scientific) and normalized to the housekeeping gene GAPDH. The comparative $2^{-\Delta\Delta CT}$ method was used for gene expression quantification, and all reactions were conducted on QuantStudio 6 or 7 platforms (Applied Biosystems, Waltham, MA).

Keratinocyte culture, treatment, RNA extraction, and qRT-PCR

Human adult primary keratinocytes (Lifeline® Cell Technology) were cultured in DermaLife Basal Medium supplement with DermaLife K LifeFactors® Kit and antibiotics [penicillin (100 U/ml), streptomycin (100 U/ml); Thermo Fisher Scientific] at 37°C, 5% CO₂. For keratinocyte treatment, the cells were plated into 24-well plates and treated with growth factors or cytokines as described in the [key resources table](#) when reaching about 70% confluency. After incubation with growth factors or cytokines for 24 hours, cells were lysed in RNAiso Plus (Takara,9109). RNA was isolated and reverse transcribed into complementary DNA using PrimeScript™ RT Master Mix (Takara, RR036A) according to the manufacturer's instructions. qRT-PCR was performed using TB Green® Premix Ex Taq™ II (Tli RNaseH Plus) (Takara, RR820A) on a Roche LightCycler®96 system. GAPDH was used as the internal control. Results were normalized to the internal control, and the comparative $2^{-\Delta\Delta CT}$ method was used to quantify gene expression.

Cell migration assay

Keratinocytes were plated into 6-well plates and treated with growth factors or cytokines as described in the [key resources table](#) when reaching about 70% confluency. After incubation with growth factors or cytokines for 24 hours, cells (95-100% confluency) were scratched using a 200 μ l pipette tip. The cells were cultured in a supplement-free medium and allowed to grow for 24 hours. Cell images at 0 h and 24 h were taken under a microscope at a magnification of $\times 10$. The cell migration rate was analyzed by measuring the healed area of the scratch using the Image J software.

Western blotting

Primary keratinocytes were plated into 6-well plates and incubated for at least 24 hours. When they reached about 70% confluency, cells were treated with 20 μ M U0126 or DMSO for 30 minutes, and then 2 ng/mL CXCL1 was added and incubated for the indicated time. Cells were lysed by RIPA lysis buffer (P0013C, Beyotime) supplemented with protease and phosphatase inhibitors on ice for 10 minutes, and the cell debris was removed by centrifugation at 12,000 rpm at 4°C for 5 minutes. The lysate was boiled with SDS loading buffer, and equal amounts of protein were loaded onto 4-20% precast polyacrylamide gels (Tanon, 180-9110H) and then transferred onto nitrocellulose membranes (Pall Corporation, 66485). The membrane was blocked with 5% non-fat powdered milk in tris-buffered saline with tween-20 (TBST). After blocking, the membrane was incubated with primary antibodies (1:1000) at 4°C overnight, washed with TBST, and incubated with HRP-labeled goat anti-rabbit secondary antibody (1:2000) (Cell Signaling Technology, 7074). Protein bands were visualized using Clarity™ Western ECL Substrate (Bio-Rad Laboratories, 170-5061). The density of protein bands was quantified using ImageJ software. GAPDH served as the loading control.

QUANTIFICATION AND STATISTICAL ANALYSIS

Softwares and statistics

The tool used to visualize acute wound scRNA-seq was adapted from the R package ShinyCell.¹²⁷ The visualization tool for the spatial data was created using the WebAtlas pipeline.¹²⁸ The workflow and schematic summary of this study were created using BioRender. Statistical significances in migration assay and immunofluorescence staining quantification between groups were determined using either a two-tailed Student's t-test or ANOVA analysis facilitated by GraphPad Prism 8 (GraphPad Software Inc, California, USA). Cell proportion and gene expression were compared between groups using a quasi-binomial distribution model and Mann-Whitney U test in R, respectively. A significance threshold of $P < 0.05$ was applied for all statistical tests. Data were presented as mean \pm standard deviation (SD) or mean \pm standard error of the mean (SEM).